Journal of Computational Physics 291 (2015) 254–278

Contents lists available at ScienceDirect

Journal of Computational Physics

www.elsevier.com/locate/jcp

A pressure correction scheme for generalized form of energy-stable open boundary conditions for incompressible flows

S. Dong *, J. Shen

Center for Computational & Applied Mathematics, Department of Mathematics, Purdue University, United States

ARTICLE INFO

Article history:
Received 22 September 2014
Received in revised form 28 January 2015
Accepted 8 March 2015
Available online 16 March 2015

Keywords:
Pressure correction scheme
Outflow
Open boundary condition
Outflow boundary condition
Unbounded domain
Backflow instability
Spectral element

ABSTRACT

We present a generalized form of open boundary conditions, and an associated numerical algorithm, for simulating incompressible flows involving open or outflow boundaries. The generalized form represents a family of open boundary conditions, which all ensure the energy stability of the system, even in situations where strong vortices or backflows occur at the open/outflow boundaries. Our numerical algorithm for treating these open boundary conditions is based on a rotational pressure correction-type strategy, with a formulation suitable for C^0 spectral-element spatial discretizations. We have introduced a discrete equation and associated boundary conditions for an auxiliary variable. The algorithm contains constructions that prevent a numerical locking at the open/outflow boundary. In addition, we have developed a scheme with a provable unconditional stability for a sub-class of the open boundary conditions. Extensive numerical experiments have been presented to demonstrate the performance of our method for several flow problems involving open/outflow boundaries. We compare simulation results with the experimental data to demonstrate the accuracy of our algorithm. Long-time simulations have been performed for a range of Reynolds numbers at which strong vortices or backflows occur at the open/outflow boundaries. We show that the open boundary conditions and the numerical algorithm developed herein produce stable simulations in such situations.

1. Introduction

Outflows or open boundaries are a crucial issue to incompressible flow simulations. Many types of flows, such as wakes, jets and shear layers, involve physically unbounded domains. To numerically simulate such problems, it is necessary to artificially truncate the domain to finite sizes. Therefore, some open boundary condition (OBC) will be required at the artificial boundary [75]. Open boundary conditions are also referred to as outflow boundary conditions or artificial boundary conditions in the literature. These boundary conditions have been under intensive studies by the community for decades, and a large volume of work has been accumulated. Some of the desirable features of an ideal method are summarized in e.g. [69]. A review of the status of the field up to the mid-1990s can be found in [69,25]; see also the references therein. Among the existing techniques the traction-free boundary condition or its variants (e.g. no-flux condition) [72,23,17,49,4,69,29,50] and the convective boundary condition [61,25,43,60,20,68,10] are some of the most commonly used. A variety

* Corresponding author.
E-mail address: sdong@purdue.edu (S. Dong).

http://dx.doi.org/10.1016/j.jcp.2015.03.012

of other methods have been contributed by various researchers; see e.g. [62,38,39,35,26,66,21,34,59,58,27,44,65,64], among others. Discussion of outflow conditions for incompressible two-phase flows has also appeared; see e.g. [12].

A commonly-encountered issue with outflows is the numerical instability associated with strong vortices or backflows at the open/outflow boundaries. It is often referred to as the backflow instability. When strong vortices or backflows occur at the open boundaries, the computation is observed to instantly become unstable (see e.g. [13,15], among others). If the Reynolds number is low, the presence of a certain amount of backflow or vortices at the open/outflow boundary usually does not cause difficulty. But when the Reynolds number increases beyond some moderate value, typically about several hundred to a thousand depending on the flow geometry, this numerical instability becomes a severe issue for simulations. It is observed that reducing the time step size or increasing the grid resolution does not help with this instability.

In production simulations a usual remedy for this problem is to employ a large computational domain for a given Reynolds number to be simulated, such that the outflow boundary can be placed far downstream and sufficiently away from the region of interest [15]. As a result, the vortices generated in the region of interest can be sufficiently dissipated before reaching the outflow boundary for the given Reynolds number. At high Reynolds numbers, the domain size essential for numerical stability can become very substantial [15]. As pointed out by [14], the drawback here is that the large computational domain requires larger meshes and induces increased computational costs. In addition, this strategy is not scalable with respect to the Reynolds number, because the domain size essential for numerical stability grows with increasing Reynolds number.

In the literature there exist several open boundary conditions that are effective for coping with the backflow instability. The earliest one appears to be from [8]; see also [9]. Based on a symmetrization of the nonlinear term and the weak form of the incompressible Navier–Stokes equation, a modified traction condition containing a term with the form ($\mathbf{n}$ denoting the directional vector at boundary and $\mathbf{u}$ denoting the velocity)

$$\frac{1}{2}(\mathbf{n}\cdot\mathbf{u})^{-}\mathbf{u}, \quad \text{where } (\mathbf{n}\cdot\mathbf{u})^{-} = \begin{cases} \mathbf{n}\cdot\mathbf{u}, & \text{if } \mathbf{n}\cdot\mathbf{u} < 0 \\ 0, & \text{otherwise} \end{cases} \tag{1}$$

was imposed on the outflow boundary in [8]. Note that the original form given in [8] includes a base velocity profile that is assumed to be known. This form of the open boundary condition has also appeared in later works by other researchers; see e.g. [48] among others. In [2,54,24,37], the traction in the open boundary condition contains a term with a similar form, $(\mathbf{n}\cdot\mathbf{u})^{-}\mathbf{u}$, but without the $\frac{1}{2}$ factor compared to [8]. Note that in [2] the boundary conditions are given separately in the normal and tangential directions, and in [54] a form $\beta(\mathbf{n}\cdot\mathbf{u})^{-}\mathbf{u}$, where $0 < \beta < 1$ is a constant, has also been considered. Based on the energy balance relation of the system, an open boundary condition is recently proposed in [14], which contains a term of the form, $\frac{1}{2}|\mathbf{u}|^2\mathbf{n}\Theta_0(\mathbf{n}\cdot\mathbf{u})$, where $\Theta_0(\mathbf{n}\cdot\mathbf{u})$ is a smoothed step function about $\mathbf{n}\cdot\mathbf{u}$ (see also Section 2.1), and $|\mathbf{u}|$ denotes the magnitude of the velocity. While the function $\Theta_0(\mathbf{n}\cdot\mathbf{u})$ plays a role comparable to that of $(\mathbf{n}\cdot\mathbf{u})^{-}$ defined in (1), the form $\frac{1}{2}|\mathbf{u}|^2\mathbf{n}$ from [14] is very different from those involving $(\mathbf{n}\cdot\mathbf{u})\mathbf{u}$ by the other researchers [8,2,54,24,37]. Another open boundary condition is proposed in a recent study [5], in which the tangential velocity derivative at the open boundary is penalized to allow for an improved energy balance.

In the current paper, we present a generalized form of the open boundary conditions that ensure the energy stability of the system. The generalized form represents a family of open boundary conditions. It contains the open boundary conditions of [8,2,24,37,14] as particular cases. In addition, it also provides new forms of energy-stable open boundary conditions. We further present an algorithm for numerically treating the generalized open boundary conditions based on a pressure correction-type strategy. It is noted that in [14] a splitting scheme based on a rotational velocity correction-type strategy [32,16] has been developed for dealing with the proposed open boundary condition therein. The numerical algorithm developed in the current work is based on a different strategy, and has a different algorithmic formulation. We refer to [30] and the references therein for a review of the pressure-correction idea and an exposition of related concepts. The main algorithm in the current paper is semi-implicit and conditionally stable in nature. In addition, we also present a rotational pressure correction scheme with a provable unconditional stability for a sub-class of the generalized open boundary conditions.

The novelties of this paper lie in three aspects: (i) the generalized form of energy-stable open boundary conditions, (ii) the rotational pressure correction-type algorithm for treating the proposed open boundary conditions, and (iii) the unconditionally stable scheme for a sub-class of the open boundary conditions.

We employ C^0 spectral elements [70,42,80] for spatial discretizations in the current paper. The algorithmic formulation presented here without change also applies to low-order finite elements. It should be noted that the open boundary conditions and the numerical algorithm for treating these boundary conditions developed herein are general, and can also be used with other spatial discretizations such as finite difference and finite volume.

2. Open boundary conditions and algorithm

2.1. A generalized form of open boundary conditions

Let Ω denote the flow domain in two or three dimensions (2-D or 3-D), and $\partial\Omega$ denote the domain boundary. We ...w contained within Ω, which is described by the normalized incompressible Navier–Stokes

$$\frac{\partial \mathbf{u}}{\partial t} + \mathbf{u}\cdot\nabla\mathbf{u} = -\nabla p + \nu\nabla^2\mathbf{u} + \mathbf{f}, \tag{2a}$$

$$\nabla\cdot\mathbf{u} = 0, \tag{2b}$$

where $\mathbf{u}(\mathbf{x},t)$ is the velocity, $p(\mathbf{x},t)$ is pressure, $\mathbf{f}(\mathbf{x},t)$ is an external body force, and $\mathbf{x}$ and t are respectively the spatial coordinate and time. $\nu = \frac{1}{Re}$ is the non-dimensional fluid viscosity, and Re is the Reynolds number defined after appropriately choosing a characteristic velocity scale and a characteristic length scale.

Let us assume that $\partial\Omega = \partial\Omega_d \cup \partial\Omega_o$, and $\partial\Omega_d \cap \partial\Omega_o = \emptyset$. $\partial\Omega_d$ is the Dirichlet boundary, on which the velocity is known,

$$\mathbf{u} = \mathbf{w}(\mathbf{x},t), \qquad \text{on } \partial\Omega_d, \tag{3}$$

where $\mathbf{w}$ is the boundary velocity. On $\partial\Omega_o$ neither the velocity $\mathbf{u}$ nor the pressure p is known. We will refer to $\partial\Omega_o$ as the open (or outflow) boundary hereafter in the paper.

We consider the following boundary conditions for the open boundary $\partial\Omega_o$,

$$\underline{\text{OBC-A}}: -p\mathbf{n} + \nu\mathbf{n}\cdot\nabla\mathbf{u} - \frac{1}{4}\left[|\mathbf{u}|^2\mathbf{n} + (\mathbf{n}\cdot\mathbf{u})\mathbf{u}\right]\Theta_0(\mathbf{n},\mathbf{u}) = \mathbf{f}_b(\mathbf{x},t), \qquad \text{on } \partial\Omega_o, \tag{4}$$

$$\underline{\text{OBC-B}}: -p\mathbf{n} + \nu\mathbf{n}\cdot\nabla\mathbf{u} - \left(|\mathbf{u}|^2\mathbf{n}\right)\Theta_0(\mathbf{n},\mathbf{u}) = \mathbf{f}_b(\mathbf{x},t), \qquad \text{on } \partial\Omega_o, \tag{5}$$

$$\underline{\text{OBC-C}}: -p\mathbf{n} + \nu\mathbf{n}\cdot\nabla\mathbf{u} - \frac{1}{2}\left[|\mathbf{u}|^2\mathbf{n} + (\mathbf{n}\cdot\mathbf{u})\mathbf{u}\right]\Theta_0(\mathbf{n},\mathbf{u}) = \mathbf{f}_b(\mathbf{x},t), \qquad \text{on } \partial\Omega_o, \tag{6}$$

where $\mathbf{n}$ is the outward-pointing unit vector normal to $\partial\Omega_o$, and $|\mathbf{u}|$ is the magnitude of the velocity $\mathbf{u}$. $\mathbf{f}_b$ is a function on $\partial\Omega_o$ for the purpose of numerical testing only, and will be set to $\mathbf{f}_b = 0$ in actual simulations. Θ_0 is a smoothed step function given by

$$\Theta_0(\mathbf{n},\mathbf{u}) = \frac{1}{2}\left(1 - \tanh\frac{\mathbf{n}\cdot\mathbf{u}}{\delta U_0}\right) \tag{7}$$

where U_0 is the characteristic velocity scale, and δ is a non-dimensional positive constant that is sufficiently small. The parameter δ controls the sharpness of the smoothed step function, and it is sharper if δ is smaller. As $\delta \to 0$, $\Theta_0(\mathbf{n},\mathbf{u})$ approaches the step function. When δ is sufficiently small, $\Theta_0(\mathbf{n},\mathbf{u})$ takes essentially the unit value where $\mathbf{n}\cdot\mathbf{u} < 0$ and vanishes otherwise. The simulation result is not sensitive to δ when it is sufficiently small; see [14].

In addition, we also consider the following conditions:

$$\underline{\text{OBC-D}}: -p\mathbf{n} + \nu\mathbf{n}\cdot\nabla\mathbf{u} - [(\mathbf{n}\cdot\mathbf{u})\mathbf{u}]\Theta_0(\mathbf{n},\mathbf{u}) = \mathbf{f}_b(\mathbf{x},t), \qquad \text{on } \partial\Omega_o, \tag{8}$$

$$\underline{\text{OBC-E}}: -p\mathbf{n} + \nu\mathbf{n}\cdot\nabla\mathbf{u} - \left(\frac{1}{2}|\mathbf{u}|^2\mathbf{n}\right)\Theta_0(\mathbf{n},\mathbf{u}) = \mathbf{f}_b(\mathbf{x},t), \qquad \text{on } \partial\Omega_o, \tag{9}$$

$$\underline{\text{OBC-F}}: -p\mathbf{n} + \nu\mathbf{n}\cdot\nabla\mathbf{u} - \left[\frac{1}{2}(\mathbf{n}\cdot\mathbf{u})\mathbf{u}\right]\Theta_0(\mathbf{n},\mathbf{u}) = \mathbf{f}_b(\mathbf{x},t), \qquad \text{on } \partial\Omega_o, \tag{10}$$

where the boundary condition (9) is developed in [14]. The condition (8) is a modified form for that of [2,24,37]. The condition (10) is a modified form based on that of [8].

These conditions belong to the following generalized form of open boundary condition

$$-p\mathbf{n} + \nu\mathbf{n}\cdot\nabla\mathbf{u} - \left[(\theta+\alpha_2)\frac{1}{2}|\mathbf{u}|^2\mathbf{n} + (1-\theta+\alpha_1)\frac{1}{2}(\mathbf{n}\cdot\mathbf{u})\mathbf{u}\right]\Theta_0(\mathbf{n},\mathbf{u}) = \mathbf{f}_b(\mathbf{x},t), \qquad \text{on } \partial\Omega_o, \tag{11}$$

where θ, α_1 and α_2 are chosen constants satisfying the conditions

$$0 \leqslant \theta \leqslant 1, \qquad \alpha_1 \geqslant 0, \qquad \alpha_2 \geqslant 0. \tag{12}$$

For example, OBC-A corresponds to (11) with $(\theta,\alpha_1,\alpha_2) = \left(\frac{1}{2},0,0\right)$, OBC-B corresponds to (11) with $(\theta,\alpha_1,\alpha_2) = (1,0,1)$, and OBC-C corresponds to (11) with $(\theta,\alpha_1,\alpha_2) = (1,1,0)$. OBC-D, OBC-E and OBC-F respectively correspond to (11) with $(\theta,\alpha_1,\alpha_2) = (0,1,0)$, $(\theta,\alpha_1,\alpha_2) = (1,0,0)$ and $(\theta,\alpha_1,\alpha_2) = (0,0,0)$.

The generalized boundary condition (11) with $\mathbf{f}_b = 0$ represents a stress balance on the outflow boundary $\partial\Omega_o$, as elaborated in [14] with the OBC-E condition. The first two terms on the left hand side (LHS) can be considered as the fluid stress on the boundary. The term involving Θ_0 is a linear combination of two effective stress forms. The term $\frac{1}{2}|\mathbf{u}|^2\mathbf{n}$ denotes an effective stress induced by the flux of kinetic energy through $\partial\Omega_o$, as discussed in [14]. The term $\frac{1}{2}(\mathbf{n}\cdot\mathbf{u})\mathbf{u}$ represents another effective stress similar in meaning, as $\left[\frac{1}{2}(\mathbf{n}\cdot\mathbf{u})\mathbf{u}\right]\cdot\mathbf{u}$ similarly denotes the kinetic energy flux through the outflow boundary. If backflow occurs on $\partial\Omega_o$, i.e. $\mathbf{n}\cdot\mathbf{u} < 0$, the generalized boundary condition (11) requires that in the ...ss should locally balance the linearly combined form of these two effective stresses.

...is in turn a special case of the following more general form of open boundary condition

$$-p\mathbf{n}+\nu\mathbf{n}\cdot\nabla\mathbf{u}-\left[\theta\frac{1}{2}|\mathbf{u}|^2\mathbf{n}+(1-\theta)\frac{1}{2}(\mathbf{n}\cdot\mathbf{u})\mathbf{u}\right.$$
$$\left.+\beta(\mathbf{n},\mathbf{u})\mathbf{n}\times\mathbf{u}-C_1(\mathbf{n},\mathbf{u})\mathbf{u}+C_2(\mathbf{n},\mathbf{u})\mathbf{n}\right]\Theta_0(\mathbf{n},\mathbf{u})=\mathbf{f}_b(\mathbf{x},t),\qquad \text{on } \partial\Omega_o, \tag{13}$$

where $\beta(\mathbf{n},\mathbf{u})$ is an arbitrary scalar function or constant, while $C_1(\mathbf{n},\mathbf{u})\geqslant 0$ and $C_2(\mathbf{n},\mathbf{u})\geqslant 0$ are two non-negative scalar functions or constants. The boundary condition (11) is obtained from (13) by letting $\beta(\mathbf{n},\mathbf{u})=0$, $C_1(\mathbf{n},\mathbf{u})=-\frac{\alpha_1}{2}(\mathbf{n}\cdot\mathbf{u})$ ($\alpha_1\geqslant 0$), and $C_2(\mathbf{n},\mathbf{u})=\frac{\alpha_2}{2}|\mathbf{u}|^2$ ($\alpha_2\geqslant 0$).

To understand the rationale underlying these boundary conditions, we consider the energy-balance equation for the system (2a)–(2b),

$$\frac{\partial}{\partial t}\int_\Omega\frac{1}{2}|\mathbf{u}|^2=-\nu\int_\Omega\|\nabla\mathbf{u}\|^2+\int_\Omega\mathbf{f}\cdot\mathbf{u}+\int_{\partial\Omega_d}\left(\mathbf{n}\cdot\mathbf{T}\cdot\mathbf{u}-\frac{1}{2}|\mathbf{u}|^2\mathbf{n}\cdot\mathbf{u}\right)+\int_{\partial\Omega_o}\left(\mathbf{n}\cdot\mathbf{T}\cdot\mathbf{u}-\frac{1}{2}|\mathbf{u}|^2\mathbf{n}\cdot\mathbf{u}\right), \tag{14}$$

where $\mathbf{T}=-p\mathbf{I}+\nu\nabla\mathbf{u}$ ($\mathbf{I}$ is the identity tensor). We assume $\mathbf{f}_b=0$ in (13) and that $\delta\to 0$ in the smoothed step function $\Theta_0(\mathbf{n},\mathbf{u})$. Employing boundary condition (13), one can then get

$$\begin{aligned}\mathbf{n}\cdot\mathbf{T}\cdot\mathbf{u}-\frac{1}{2}|\mathbf{u}|^2\mathbf{n}\cdot\mathbf{u}&=(-p\mathbf{n}+\nu\mathbf{n}\cdot\nabla\mathbf{u})\cdot\mathbf{u}-\frac{1}{2}|\mathbf{u}|^2\mathbf{n}\cdot\mathbf{u}\\&=\begin{cases}-C_1|\mathbf{u}|^2+C_2(\mathbf{n}\cdot\mathbf{u}), & \text{if } \mathbf{n}\cdot\mathbf{u}<0,\\ -\frac{1}{2}|\mathbf{u}|^2(\mathbf{n}\cdot\mathbf{u}), & \text{if } \mathbf{n}\cdot\mathbf{u}\geqslant 0,\end{cases}\qquad \text{on } \partial\Omega_o,\quad \text{as } \delta\to 0.\end{aligned} \tag{15}$$

Therefore, with the boundary condition (13), the last surface integral over the open boundary $\partial\Omega_o$ in the energy balance equation (14) will always be non-positive if δ is sufficiently small. This ensures the energy stability of the system (in the absence of external forces), even if there exists backflow or energy influx (i.e. $\mathbf{n}\cdot\mathbf{u}<0$) into the domain through the open boundary $\partial\Omega_o$. It should be noted that these boundary conditions are given in the reference frame in which the domain Ω is fixed in time. They are not for arbitrary reference frames.

Apart from the boundary conditions, we assume the following initial condition for the velocity

$$\mathbf{u}(\mathbf{x},t=0)=\mathbf{u}_{in}(\mathbf{x}), \tag{16}$$

where $\mathbf{u}_{in}$ is the initial velocity field satisfying Eq. (2b) and compatible with the boundary condition (3).

The governing equations (2a) and (2b), supplemented by the boundary condition (3) on $\partial\Omega_d$ and an open boundary condition (among Eqs. (4)–(6), or (8)–(10), or (11)) on $\partial\Omega_o$, together with the initial condition (16) for the velocity, constitute the system to be solved in numerical simulations.

2.2. Algorithm formulation

In this section we present an algorithm based on a pressure correction-type strategy for solving the governing equations together with the boundary conditions discussed above. Our emphasis here is on the numerical treatment of the open boundary conditions.

To facilitate subsequent discussions, we re-write the open boundary condition (11) in a more compact form as follows:

$$-p\mathbf{n}+\nu\mathbf{n}\cdot\nabla\mathbf{u}-\mathbf{E}(\mathbf{n},\mathbf{u})=\mathbf{f}_b(\mathbf{x},t),\qquad \text{on } \partial\Omega_o, \tag{17}$$

where

$$\mathbf{E}(\mathbf{n},\mathbf{u})=\left[(\theta+\alpha_2)\frac{1}{2}|\mathbf{u}|^2\mathbf{n}+(1-\theta+\alpha_1)\frac{1}{2}(\mathbf{n}\cdot\mathbf{u})\mathbf{u}\right]\Theta_0(\mathbf{n},\mathbf{u}). \tag{18}$$

The system to solve consists of Eqs. (2a) and (2b), together with the boundary conditions (3) and (17).

Let n ($n\geqslant 0$) denote the time step index, and $(\cdot)^n$ denote the variable $(\cdot)$ at time step n. We use $\tilde{\mathbf{u}}^n$ and $\mathbf{u}^n$ to denote two slightly different approximations of the velocity $\mathbf{u}$ at step n. Define

$$\tilde{\mathbf{u}}^0=\mathbf{u}_{in},\quad \mathbf{u}^0=\mathbf{u}_{in}. \tag{19}$$

Let $H^1_{p0}(\Omega)=\left\{v\in H^1(\Omega)\ :\ v|_{\partial\Omega_o}=0\right\}$. By enforcing Eq. (2a) at $t=0$ and using Eqs. (2b) and (3), we obtain an equation in weak form about the initial pressure p^0,

$$\int_\Omega\nabla p^0\cdot\nabla q=\int_\Omega\left(\mathbf{f}^0-\mathbf{u}_{in}\cdot\nabla\mathbf{u}_{in}\right)\cdot\nabla q-\nu\int_{\partial\Omega_d\cup\partial\Omega_o}\mathbf{n}\times(\nabla\times\mathbf{u}_{in})\cdot\nabla q-\int_{\partial\Omega_d}\mathbf{n}\cdot\left.\frac{\partial\mathbf{w}}{\partial t}\right|^0 q,\quad \forall q\in H^1_{p0}(\Omega), \tag{20}$$

where q is a test function and $\mathbf{n}$ is the outward-pointing unit vector normal to $\partial\Omega$. $\left.\frac{\partial\mathbf{w}}{\partial t}\right|^0$ denotes $\frac{\partial\mathbf{w}}{\partial t}$ at time step zero, and … (e.g. by the second-order backward differentiation formula) because the boundary velocity … uation can be solved for p^0, together with the following pressure Dirichlet condition

$$p^0 = \nu \mathbf{n} \cdot \nabla \mathbf{u}_{in} \cdot \mathbf{n} - \mathbf{n} \cdot \mathbf{E}(\mathbf{n}, \mathbf{u}_{in}) - \mathbf{f}_b^0 \cdot \mathbf{n}, \quad \text{on } \partial\Omega_o. \tag{21}$$

Given ($\tilde{\mathbf{u}}^n$, $\mathbf{u}^n$, p^n), we compute ($\tilde{\mathbf{u}}^{n+1}$, p^{n+1}, $\mathbf{u}^{n+1}$), together with an auxiliary scalar field variable ϕ^{n+1}, successively in a de-coupled fashion as follows:
<u>For $\tilde{\mathbf{u}}^{n+1}$:</u>

$$\frac{\gamma_0 \tilde{\mathbf{u}}^{n+1} - \hat{\mathbf{u}}}{\Delta t} + \tilde{\mathbf{u}}^{*,n+1} \cdot \nabla \tilde{\mathbf{u}}^{*,n+1} + \nabla p^n - \nu \nabla^2 \tilde{\mathbf{u}}^{n+1} = \mathbf{f}^{n+1}, \tag{22a}$$

$$\tilde{\mathbf{u}}^{n+1} = \mathbf{w}^{n+1}, \quad \text{on } \partial\Omega_d, \tag{22b}$$

$$\mathbf{n} \cdot \nabla \tilde{\mathbf{u}}^{n+1} = \frac{1}{\nu} \left[p^{*,n+1} \mathbf{n} + \mathbf{E}(\mathbf{n}, \tilde{\mathbf{u}}^{*,n+1}) + \mathbf{f}_b^{n+1} \right], \quad \text{on } \partial\Omega_o. \tag{22c}$$

<u>For ϕ^{n+1}:</u>

$$\frac{\gamma_0}{\Delta t} \phi^{n+1} - \nu \nabla^2 \phi^{n+1} = \nabla \cdot \left[\mathbf{f}^{n+1} - \tilde{\mathbf{u}}^{*,n+1} \cdot \nabla \tilde{\mathbf{u}}^{*,n+1} - \nabla p^n \right], \tag{23a}$$

$$\mathbf{n} \cdot \nabla \phi^{n+1} = \frac{1}{\nu} \mathbf{n} \cdot \frac{\gamma_0 \mathbf{w}^{n+1} - \hat{\mathbf{w}}}{\Delta t} - \frac{1}{\nu} \mathbf{n} \cdot \left[\mathbf{f}^{n+1} - \tilde{\mathbf{u}}^{*,n+1} \cdot \nabla \tilde{\mathbf{u}}^{*,n+1} - \nabla p^n \right] + \mathbf{n} \cdot \nabla \times \tilde{\boldsymbol{\omega}}^{n+1}, \quad \text{on } \partial\Omega_d, \tag{23b}$$

$$\phi^{n+1} = \nabla \cdot \tilde{\mathbf{u}}^{n+1}, \quad \text{on } \partial\Omega_o. \tag{23c}$$

<u>For p^{n+1}:</u>

$$\frac{\gamma_0 \mathbf{u}^{n+1} - \gamma_0 \tilde{\mathbf{u}}^{n+1}}{\Delta t} + \nabla \left(p^{n+1} - p^n + \nu \phi^{n+1} \right) = 0, \tag{24a}$$

$$\nabla \cdot \mathbf{u}^{n+1} = 0, \tag{24b}$$

$$\mathbf{n} \cdot \mathbf{u}^{n+1} = \mathbf{n} \cdot \mathbf{w}^{n+1}, \quad \text{on } \partial\Omega_d, \tag{24c}$$

$$p^{n+1} = \nu \mathbf{n} \cdot \nabla \tilde{\mathbf{u}}^{n+1} \cdot \mathbf{n} - \mathbf{n} \cdot \mathbf{E}\left(\mathbf{n}, \tilde{\mathbf{u}}^{n+1} \right) - \mathbf{f}_b^{n+1} \cdot \mathbf{n} - \nu \phi^{n+1}, \quad \text{on } \partial\Omega_o. \tag{24d}$$

<u>For $\mathbf{u}^{n+1}$:</u>

$$\mathbf{u}^{n+1} = \tilde{\mathbf{u}}^{n+1} - \frac{\Delta t}{\gamma_0} \nabla \left(p^{n+1} - p^n + \nu \phi^{n+1} \right). \tag{25}$$

The meanings of the symbols involved in the above Eqs. (22a)–(25) are as follows. Δt denotes the time step size. Let J ($J = 1$ or 2) denote the temporal order of the scheme. Then $\tilde{\mathbf{u}}^{*,n+1}$ and $p^{*,n+1}$ respectively denote the J-th order explicit approximations of $\tilde{\mathbf{u}}^{n+1}$ and p^{n+1}, given by

$$\tilde{\mathbf{u}}^{*,n+1} = \begin{cases} \tilde{\mathbf{u}}^n, & J = 1, \\ 2\tilde{\mathbf{u}}^n - \tilde{\mathbf{u}}^{n-1}, & J = 2, \end{cases} \qquad p^{*,n+1} = \begin{cases} p^n, & J = 1, \\ 2p^n - p^{n-1}, & J = 2. \end{cases} \tag{26}$$

$\hat{\mathbf{u}}$ and the constant γ_0 are given by

$$\hat{\mathbf{u}} = \begin{cases} \mathbf{u}^n, & J = 1, \\ 2\mathbf{u}^n - \frac{1}{2}\mathbf{u}^{n-1}, & J = 2, \end{cases} \qquad \gamma_0 = \begin{cases} 1, & J = 1, \\ \frac{3}{2}, & J = 2. \end{cases} \tag{27}$$

$\mathbf{w}$ is the boundary velocity on $\partial\Omega_d$, and $\hat{\mathbf{w}}$ is defined in the same way as $\hat{\mathbf{u}}$ defined above. The auxiliary variable ϕ^{n+1} represents an approximation of the quantity $\nabla \cdot \tilde{\mathbf{u}}^{n+1}$. $\mathbf{n}$ is the outward-pointing unit vector normal to the boundary. $\tilde{\boldsymbol{\omega}}^{n+1}$ denotes the vorticity, $\tilde{\boldsymbol{\omega}}^{n+1} = \nabla \times \tilde{\mathbf{u}}^{n+1}$. $\mathbf{E}(\mathbf{n}, \mathbf{u})$ is defined in Eq. (18).

One can recognize that the overall structure of the above algorithm resembles a rotational incremental pressure correction-type strategy (see [30]). Two features distinguish the above scheme from the usual pressure correction formulations. One feature lies in the introduction of Eq. (23a) for the variable ϕ^{n+1} and the associated boundary conditions (23b) and (23c). One can note that this equation for ϕ^{n+1} exists only in the discrete sense, and it differs from the dynamic equation about $\nabla \cdot \mathbf{u}$ at the continuum level. Another aspect that this scheme differs from the usual formulation lies in the form of the second term on the left hand side (LHS) of Eq. (24a). This form allows us to compute the pressure p^{n+1} directly in the $H^1(\Omega)$ space. On the other hand, one notes that with the usual rotational pressure-correction formulation [73,30] the pressure p^{n+1} resides in the $L^2(\Omega)$ space. More importantly, this form allows for a straightforward discrete pressure condition (see (24d)) on the open domain boundary. We would like to point out that the purpose of Eq. (25) is for the evaluation of $\mathbf{u}^{n+1}$ in the $L^2(\Omega)$ space, not for the projection to the $H^1(\Omega)$ space.

We briefly mention some variants to the treatment of the governing equations. An alternative to the ϕ^{n+1} step (Eqs. (23a)–(23c)) of the above algorithm is the following,

(28)

This amounts to a projection of $\nabla\cdot\tilde{\mathbf{u}}$ to the $H^1(\Omega)$ space, and requires the solution of a linear algebraic system involving the global mass matrix. The computational costs for solving (28) and for solving (23a)–(23c) are comparable. However, we observe that the algorithm using Eqs. (23a)–(23c) provides consistently improved accuracy for the pressure than that using (28). In Eqs. (23a)–(23b), replacing $\tilde{\mathbf{u}}^{*,n+1}\cdot\nabla\tilde{\mathbf{u}}^{*,n+1}$ by $\tilde{\mathbf{u}}^{n+1}\cdot\nabla\tilde{\mathbf{u}}^{n+1}$ makes little difference in terms of stability and accuracy in numerical simulations. However, it increases the computational cost to a certain extent because of the need for the extra computation of $\tilde{\mathbf{u}}^{n+1}\cdot\nabla\tilde{\mathbf{u}}^{n+1}$.

Let us now comment on the numerical treatments of the boundary conditions. In the velocity substep for $\tilde{\mathbf{u}}^{n+1}$, we have imposed a velocity Neumann-type condition (22c) on $\partial\Omega_o$, which is derived from the open boundary condition (17). The pressure and velocity are treated explicitly in this Neumann condition. A variant form for the velocity Neumann condition (22c) is

$$\mathbf{n}\cdot\nabla\tilde{\mathbf{u}}^{n+1}=\frac{1}{\nu}\left[p^n\mathbf{n}+\mathbf{E}(\mathbf{n},\tilde{\mathbf{u}}^{*,n+1})+\mathbf{f}_b^{n+1}\right],\qquad \text{on } \partial\Omega_o, \tag{29}$$

which is also observed to be stable. When solving for ϕ^{n+1}, we have imposed a Neumann-type condition (23b) on $\partial\Omega_d$ and Dirichlet-type condition (23c) on $\partial\Omega_o$. In the pressure substep for p^{n+1}, a pressure Dirichlet-type condition (24d) has been imposed on the open boundary $\partial\Omega_o$. This pressure condition is essentially obtained from the open boundary condition (17), by taking the inner product between this equation and $\mathbf{n}$, and it contains an extra term $-\nu\phi^{n+1}$. The velocity in the pressure Dirichlet condition is approximated using $\tilde{\mathbf{u}}^{n+1}$ computed from a previous substep. A variant form of the pressure Dirichlet condition (24d) is the following,

$$p^{n+1}=\nu\mathbf{n}\cdot\nabla\tilde{\mathbf{u}}^{n+1}\cdot\mathbf{n}-\mathbf{n}\cdot\mathbf{E}\left(\mathbf{n},\tilde{\mathbf{u}}^{n+1}\right)-\mathbf{f}_b^{n+1}\cdot\mathbf{n}-\nu\nabla\cdot\tilde{\mathbf{u}}^{n+1},\quad \text{on } \partial\Omega_o, \tag{30}$$

which is also observed to be stable. Note that the discrete formulations (24d) and (30) are numerically not equivalent, because of the need for a projection to the $H^1(\partial\Omega_o)$ space (to be discussed below) when imposing the Dirichlet condition (23c) for ϕ^{n+1} on $\partial\Omega_o$.

The construction $-\nu\phi^{n+1}$ in (24d) (or $-\nu\nabla\cdot\tilde{\mathbf{u}}^{n+1}$ in (30)) is crucial to the current algorithm. If this term is absent, assuming $\mathbf{f}_b=0$ and that no backflow occurs at the outflow boundary (i.e. $\mathbf{n}\cdot\mathbf{u}\geqslant 0$), then by combining Eqs. (22c) and (24d) one can show that

$$p^{n+1}|_{\partial\Omega_o}=p^n|_{\partial\Omega_o}=\cdots=p^0|_{\partial\Omega_o},\quad \mathbf{n}\cdot\nabla\tilde{\mathbf{u}}^{n+1}|_{\partial\Omega_o}=\mathbf{n}\cdot\nabla\tilde{\mathbf{u}}^{n}|_{\partial\Omega_o}=\cdots=\mathbf{n}\cdot\nabla\tilde{\mathbf{u}}^{0}|_{\partial\Omega_o}, \tag{31}$$

leading to a numerical locking at the open boundary $\partial\Omega_o$.

2.3. Implementation with C^0 spectral elements

We employ high-order spectral element methods [70,42,80] for spatial discretizations in the current paper. Let us next discuss how to implement the algorithm, (22a)–(25), using C^0-continuous spectral elements. The formulations given below without change can also be applied to low-order finite element methods.

The main issues are posed by the terms such as $\nabla\cdot\left(\tilde{\mathbf{u}}^{*,n+1}\cdot\nabla\tilde{\mathbf{u}}^{*,n+1}\right)$ in (23a) and $\nabla\times\tilde{\boldsymbol{\omega}}^{n+1}$ in (23b), which cannot be readily computed in the discrete function space with C^0 elements. We will derive the weak formulations for the algorithm, and in the process treat the trouble terms in an appropriate fashion.

Let $H^1_{u0}(\Omega)=\left\{v\in H^1(\Omega)\ :\ v|_{\partial\Omega_d}=0\right\}$, and $\varphi\in H^1_{u0}(\Omega)$ denote the test function. By taking the L^2 inner product between φ and Eq. (22a), and integrating by part, on can obtain the weak form for $\tilde{\mathbf{u}}^{n+1}$,

$$\begin{aligned}
&\frac{\gamma_0}{\nu\Delta t}\int_\Omega \varphi\tilde{\mathbf{u}}^{n+1}+\int_\Omega \nabla\varphi\cdot\nabla\tilde{\mathbf{u}}^{n+1}\\
&=\frac{1}{\nu}\int_\Omega\left[\mathbf{f}^{n+1}-\tilde{\mathbf{u}}^{*,n+1}\cdot\nabla\tilde{\mathbf{u}}^{*,n+1}-\nabla p^n+\frac{\hat{\mathbf{u}}}{\Delta t}\right]\varphi\\
&\quad+\frac{1}{\nu}\int_{\partial\Omega_o}\left[p^{*,n+1}\mathbf{n}+\mathbf{E}(\mathbf{n},\tilde{\mathbf{u}}^{*,n+1})+\mathbf{f}_b^{n+1}\right]\varphi,\qquad \forall\varphi\in H^1_{u0}(\Omega),
\end{aligned} \tag{32}$$

where we have used the boundary condition (22c), and the fact that $\int_{\partial\Omega_d}\mathbf{n}\cdot\nabla\tilde{\mathbf{u}}^{n+1}\varphi=0$ because $\varphi\in H^1_{u0}(\Omega)$.

Let $\vartheta\in H^1_{p0}(\Omega)$ denote a test function. By taking the L^2 inner product between ϑ and Eq. (23a) and integrating by part, we can get the weak form about ϕ^{n+1},

$$\frac{\gamma_0}{\nu\Delta t}\int_\Omega \phi^{n+1}\vartheta+\int_\Omega\nabla\phi^{n+1}\cdot\nabla\vartheta$$

$$\cdots{}^{n+1}\cdot\nabla\tilde{\mathbf{u}}^{*,n+1}-\nabla p^n\Big]\cdot\nabla\vartheta$$

$$+\frac{1}{\nu}\int\limits_{\partial\Omega_d}\mathbf{n}\cdot\frac{\gamma_0\mathbf{w}^{n+1}-\hat{\mathbf{w}}}{\Delta t}\vartheta+\int\limits_{\partial\Omega_d}\mathbf{n}\times\tilde{\boldsymbol{\omega}}^{n+1}\cdot\nabla\vartheta+\int\limits_{\partial\Omega_o}\mathbf{n}\times\tilde{\boldsymbol{\omega}}^{n+1}\cdot\nabla\vartheta,\quad\forall\vartheta\in H_{p0}(\Omega),\tag{33}$$

where we have used the divergence theorem, the boundary condition (23b), and the following identity,

$$\begin{aligned}\int\limits_{\partial\Omega_d}\mathbf{n}\cdot\nabla\times\tilde{\boldsymbol{\omega}}^{n+1}\vartheta&=\int\limits_{\partial\Omega}\mathbf{n}\cdot\nabla\times\tilde{\boldsymbol{\omega}}^{n+1}\vartheta=\int\limits_{\Omega}\nabla\times\tilde{\boldsymbol{\omega}}^{n+1}\cdot\nabla\vartheta=\int\limits_{\Omega}\nabla\cdot\left(\tilde{\boldsymbol{\omega}}^{n+1}\times\nabla\vartheta\right)\\&=\int\limits_{\partial\Omega}\mathbf{n}\times\tilde{\boldsymbol{\omega}}^{n+1}\cdot\nabla\vartheta,\qquad\forall\vartheta\in H_{p0}(\Omega).\end{aligned}\tag{34}$$

Let $q\in H^1_{p0}(\Omega)$ denote the test function. Taking the L^2 inner product between Eq. (24a) and ∇q, and integrating by part, we obtain the weak form for p^{n+1}

$$\int\limits_{\Omega}\nabla p^{n+1}\cdot\nabla q=\int\limits_{\Omega}\left[\frac{\gamma_0}{\Delta t}\tilde{\mathbf{u}}^{n+1}+\nabla\left(p^n-\nu\phi^{n+1}\right)\right]\cdot\nabla q-\frac{\gamma_0}{\Delta t}\int\limits_{\partial\Omega_d}\mathbf{n}\cdot\mathbf{w}^{n+1}q,\qquad\forall q\in H^1_{p0}(\Omega),\tag{35}$$

where we have used Eqs. (24b) and (24c), and the fact that $\int_{\partial\Omega_o}\mathbf{n}\cdot\mathbf{u}^{n+1}q=0$ because $q\in H^1_{p0}(\Omega)$.

The weak formulations (32), (33) and (35) contain no complicating terms with derivatives of order two or higher. All terms involved therein can be computed directly in the discrete space of C^0 elements. These weak forms can be discretized using C^0 spectral elements (or finite elements).

Let Ω_h denote the domain Ω partitioned using a spectral element mesh, and $\partial\Omega_h$ denote the boundary of Ω_h, $\partial\Omega_h=\partial\Omega_{dh}\cup\partial\Omega_{oh}$, where $\partial\Omega_{dh}$ and $\partial\Omega_{oh}$ are respectively the discretized $\partial\Omega_d$ and $\partial\Omega_o$. We use $X_h\subset[H^1(\Omega_h)]^d$ ($d=2$ or 3 is the spatial dimension) to denote the approximation space for the velocity $\tilde{\mathbf{u}}_h^{n+1}$, and $M_h\subset H^1(\Omega_h)$ to denote the approximation space for the pressure p_h^{n+1} and the field variable ϕ_h^{n+1}. Let $X_{h0}=\{v\in H^1(\Omega_h)\ :\ v|_{\partial\Omega_{dh}}=0\}$, and $M_{h0}=\{v\in M_h\ :\ v|_{\partial\Omega_{oh}}=0\}$. Then the fully discretized equations for (32) and (22b) are: find $\tilde{\mathbf{u}}_h^{n+1}\in X_h$ such that

$$\begin{aligned}\frac{\gamma_0}{\nu\Delta t}\int\limits_{\Omega_h}\varphi_h\tilde{\mathbf{u}}_h^{n+1}+\int\limits_{\Omega_h}\nabla\varphi_h\cdot\nabla\tilde{\mathbf{u}}_h^{n+1}&=\frac{1}{\nu}\int\limits_{\Omega_h}\left[\mathbf{f}_h^{n+1}-\tilde{\mathbf{u}}_h^{*,n+1}\cdot\nabla\tilde{\mathbf{u}}_h^{*,n+1}-\nabla p_h^n+\frac{\hat{\mathbf{u}}_h}{\Delta t}\right]\varphi_h\\&\quad+\frac{1}{\nu}\int\limits_{\partial\Omega_{oh}}\left[p_h^{*,n+1}\mathbf{n}_h+\mathbf{E}(\mathbf{n}_h,\tilde{\mathbf{u}}_h^{*,n+1})+\mathbf{f}_{bh}^{n+1}\right]\varphi_h,\qquad\forall\varphi_h\in X_{h0},\end{aligned}\tag{36}$$

and

$$\tilde{\mathbf{u}}_h^{n+1}=\mathbf{w}_h,\quad\text{on }\partial\Omega_{dh},\tag{37}$$

where the subscript $(\cdot)_h$ represents the discretized version of $(\cdot)$. The fully discretized equations for (33) and (23c) are: find $\phi_h^{n+1}\in M_h$ such that

$$\begin{aligned}&\frac{\gamma_0}{\nu\Delta t}\int\limits_{\Omega_h}\phi_h^{n+1}\vartheta_h+\int\limits_{\Omega_h}\nabla\phi_h^{n+1}\cdot\nabla\vartheta_h\\&\quad=-\frac{1}{\nu}\int\limits_{\Omega_h}\left[\mathbf{f}_h^{n+1}-\tilde{\mathbf{u}}_h^{*,n+1}\cdot\nabla\tilde{\mathbf{u}}_h^{*,n+1}-\nabla p_h^n\right]\cdot\nabla\vartheta_h\\&\qquad+\frac{1}{\nu}\int\limits_{\partial\Omega_{dh}}\mathbf{n}_h\cdot\frac{\gamma_0\mathbf{w}_h^{n+1}-\hat{\mathbf{w}}_h}{\Delta t}\vartheta_h+\int\limits_{\partial\Omega_{dh}\cup\partial\Omega_{oh}}\mathbf{n}_h\times\tilde{\boldsymbol{\omega}}_h^{n+1}\cdot\nabla\vartheta_h,\quad\forall\vartheta_h\in M_{h0},\end{aligned}\tag{38}$$

and

$$\phi_h^{n+1}=\nabla\cdot\tilde{\mathbf{u}}_h^{n+1},\quad\text{on }\partial\Omega_{oh}.\tag{39}$$

The fully discretized equations of (35) and (24d) are: find $p_h^{n+1}\in M_h$ such that

$$\int\limits_{\Omega_h}\nabla p_h^{n+1}\cdot\nabla q_h=\int\limits_{\Omega_h}\left[\frac{\gamma_0}{\Delta t}\tilde{\mathbf{u}}_h^{n+1}+\nabla\left(p_h^n-\nu\phi_h^{n+1}\right)\right]\cdot\nabla q_h-\frac{\gamma_0}{\Delta t}\int\limits_{\partial\Omega_{dh}}\mathbf{n}_h\cdot\mathbf{w}_h^{n+1}q_h,\quad\forall q_h\in M_{h0},\tag{40}$$

and

$$\ldots\mathbf{n}_h\cdot\mathbf{E}\left(\mathbf{n}_h,\tilde{\mathbf{u}}_h^{n+1}\right)-\mathbf{f}_{bh}^{n+1}\cdot\mathbf{n}_h-\nu\phi_h^{n+1},\quad\text{on }\partial\Omega_{oh}.\tag{41}$$

In addition, $\mathbf{u}_h^{n+1}$ is evaluated by the following discretized version of Eq. (25),

$$\mathbf{u}_h^{n+1} = \tilde{\mathbf{u}}_h^{n+1} - \frac{\Delta t}{\gamma_0}\nabla\left(p_h^{n+1} - p_h^n + \nu\phi_h^{n+1}\right). \tag{42}$$

The final solution procedure can therefore be summarized as follows. Given ($\tilde{\mathbf{u}}_h^n$, $\mathbf{u}_h^n$, p_h^n), we employ the following steps to compute the variables at time step $(n+1)$:

- Solve Eq. (36), together with the velocity Dirichlet condition (37) on $\partial\Omega_{dh}$, for $\tilde{\mathbf{u}}_h^{n+1}$;
- Solve Eq. (38), together with the Dirichlet condition (39) for ϕ_h^{n+1} on $\partial\Omega_{oh}$, for ϕ_h^{n+1};
- Solve Eq. (40), together with the pressure Dirichlet condition (41) on $\partial\Omega_{oh}$, for p_h^{n+1};
- Evaluate $\mathbf{u}_h^{n+1}$ based on Eq. (42), using $\tilde{\mathbf{u}}_h^{n+1}$, ϕ_h^{n+1} and p_h^{n+1} computed above.

It can be observed that in Eq. (36) different components of the velocity $\tilde{\mathbf{u}}_h^{n+1}$ are not coupled and therefore can be computed individually.

We briefly comment on how to impose the Dirichlet conditions for ϕ_h^{n+1} and p_h^{n+1} on the open boundary $\partial\Omega_{oh}$ in the second and third steps of the above algorithm. The expressions for the boundary conditions (39) and (41) both involve derivatives of the velocity $\tilde{\mathbf{u}}_h^{n+1}$. Consequently, the Dirichlet data for ϕ_h^{n+1} and p_h^{n+1} on $\partial\Omega_{oh}$ computed from (39) and (41) may not be continuous across the element boundaries on $\partial\Omega_{oh}$ with C^0 spectral elements (or finite elements). Therefore, when imposing these Dirichlet conditions, one needs to first project the Dirichlet data computed from (39) and (41) into the $H^1(\partial\Omega_{oh})$ space, and then use the projected data for the Dirichlet conditions on $\partial\Omega_{oh}$. This projection essentially amounts to solving a small linear algebraic system with the coefficient matrix being the mass matrix on $\partial\Omega_{oh}$. If $\partial\Omega_{oh}$ consists of several disjoint pieces, the projection can be performed on each individual piece separately.

As is well-known, the approximation spaces for the discrete velocity and pressure should satisfy an inf–sup condition for compatibility, otherwise spurious pressure modes may result; see e.g. [47,1,7,28,30,18] among others, and also the references therein. On the other hand, substantial evidence exists based on the works of a number of researchers that several types of schemes can work properly with approximation spaces that do not satisfy the usual inf–sup condition, e.g. with the equal-order approximation for the velocity and pressure; see e.g. [41,73,31,42,30,51,50,16,14] among others. Extensive numerical experiments of ours show that the current splitting scheme represented by Eqs. (36)–(42) using spectral element discretizations can work properly with equal-order approximations for the velocity and the pressure. No spurious modes for the pressure are observed. In the current implementation and in all the flow tests of Section 3, we have used the same orders of expansion polynomials to approximate the velocity and the pressure in the spectral element discretization.

There are two approximations, $\tilde{\mathbf{u}}^n$ and $\mathbf{u}^n$, for the velocity from the above algorithm. The issue of which one to use in simulations has been discussed in detail by [30]. As shown by the analysis of [33] and pointed out by [30], the two approximation velocities have the same error estimates and in terms of accuracy there is no reason for preferring one to the other. In the current paper we will use the approximation velocity $\tilde{\mathbf{u}}^n$ when presenting results. All the results in Section 3 regarding the velocity are with $\tilde{\mathbf{u}}^n$.

3. Representative numerical examples

In this section we use several flow problems in two dimensions (2-D) involving inflow/outflow boundaries to demonstrate the performance of the numerical algorithm and the effectiveness of the open boundary conditions developed in the previous section. The flow regimes covered by the 2-D simulations range from low to quite high Reynolds numbers, at which strong backflows or vortices occur at the outflow/open boundaries and the physical flow in reality would have become three-dimensional. We compare our simulation results with experimental data and also with the other numerical simulations from the literature.

3.1. Convergence rates

3.1.1. Contrived flow with analytic solution

The goal of this subsection is to use an unsteady analytic flow problem to show the spatial and temporal convergence rates of the method developed here.

We consider the rectangular flow domain $\overline{ABCD}$ as sketched in Fig. 1(a), $0 \leqslant x \leqslant 2$ and $-1 \leqslant y \leqslant 1$, and the following analytic expressions for the flow variables

$$\begin{cases} u = A\cos\pi y \sin ax \sin bt, \\ v = -\dfrac{Aa}{\pi}\sin\pi y \cos ax \sin bt, \\ p = A\sin\pi y \sin ax \cos bt, \end{cases} \tag{43}$$

where (u, v) are the x and y components of the velocity $\mathbf{u}$, and A, a and b are prescribed constants whose values are to be ... expression satisfies the continuity equation (2b). The external body force $\mathbf{f}(\mathbf{x}, t)$ in (2a) is ... in (43) satisfy Eq. (2a).

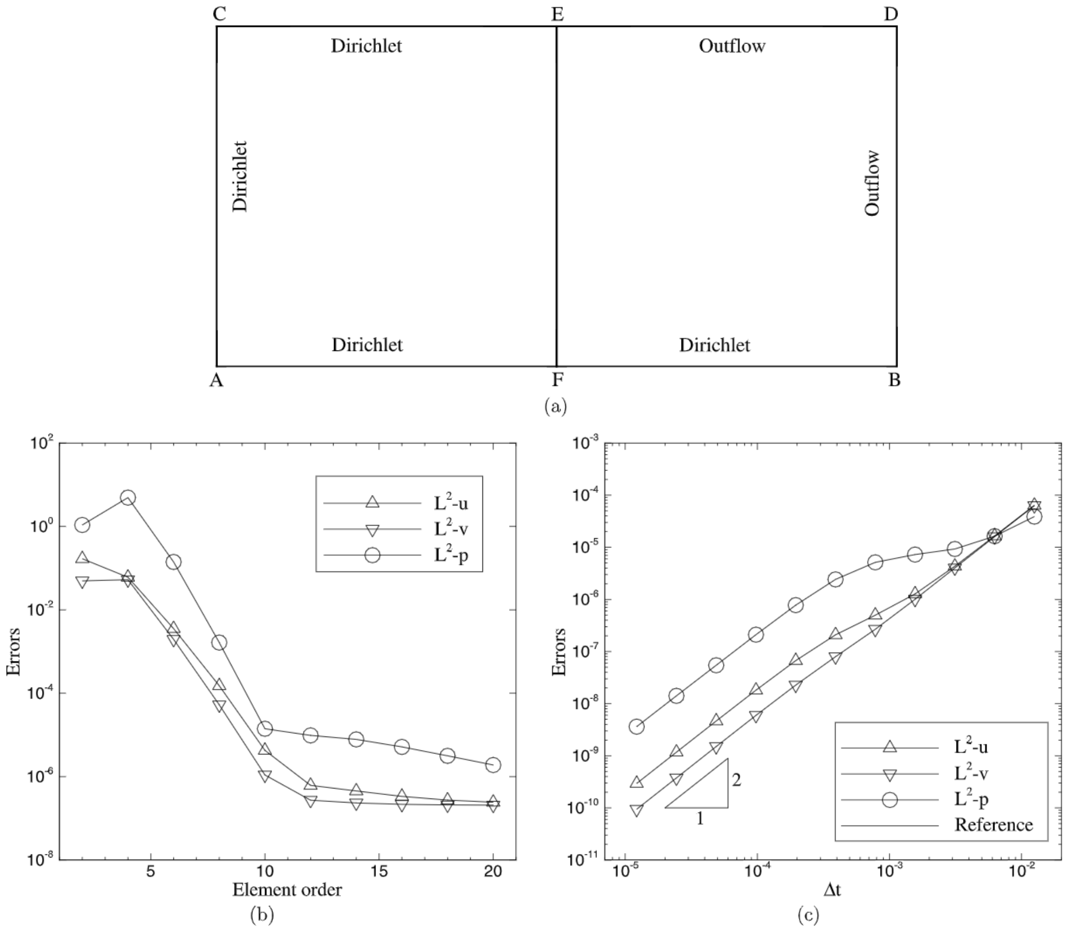

Fig. 1. Spatial and temporal convergence rates: (a) Flow configuration and boundary conditions; L^2 errors of the flow variables as a function of the element order (b), and as a function of the time step size Δt (c). In (b) the time step size is fixed at $\Delta t = 0.001$. In (c) the element order is fixed at 18. Results are obtained with the OBC-E outflow boundary condition.

Table 1
Physical and numerical parameters for convergence-rate tests.

Parameter	Value	Parameter	Value
A	2.0	δ	0.05
a	π	U_0	1.0
b	1.0	J (temporal order)	2
ν	0.01		

The domain is partitioned into two equal-sized spectral elements $\overline{AFEC}$ and $\overline{FBDE}$ along the x direction, see Fig. 1(a). On the faces $\overline{AB}$, $\overline{AC}$ and $\overline{CE}$ the velocity Dirichlet boundary condition (3) is imposed, where the boundary velocity $\mathbf{w}$ is chosen according to the analytical expression from (43). On the faces $\overline{BD}$ and $\overline{DE}$ the outflow boundary condition (17) is imposed, where $\mathbf{f}_b$ is chosen such that the analytic expressions in (43) satisfy Eq. (17) on these boundaries.

We employ the algorithm presented in Section 2.2 to integrate the Navier–Stokes equations in time from $t = 0$ to $t = t_f$ (t_f is the final time to be given below), and then compute the errors of the numerical solution at $t = t_f$ against the analytic solution given in (43). The element order or the time step size Δt is varied systematically, and the numerical errors are monitored. Table 1 lists the physical and numerical parameters involved in this problem.

In the first group of tests, we fix the time step size at $\Delta t = 0.001$ and the final integration time at $t_f = 0.1$ (i.e. 100 time steps), and vary the element order systematically from 2 to 20. Fig. 1(b) shows the L^2 errors of the flow variables at $t = t_f$ as a function of the element order. These results are obtained with the outflow boundary condition OBC-E, corresponding to the parameters $(\theta, \alpha_1, \alpha_2) = (1, 0, 0)$. One can observe that the errors decrease exponentially as the element order increases while below order 10. As the element order increases further beyond 12, the errors remain essentially constant or decrease ...turation by the temporal truncation errors. These results demonstrate the spatial exponential ...hod.

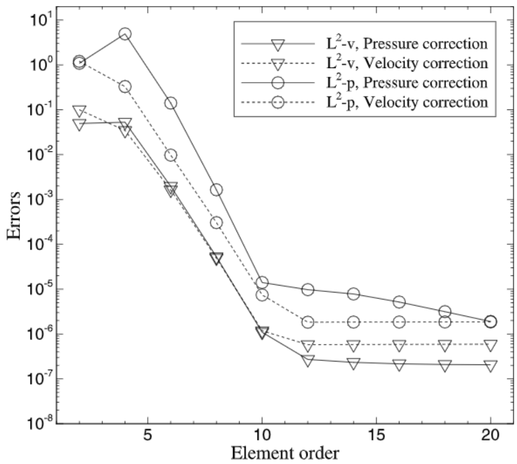

Fig. 2. Comparison between pressure-correction and velocity-correction schemes: L^2 errors of velocity and pressure as a function of the element order (fixed $\Delta t = 0.001$). Results correspond to the OBC-E outflow condition.

In the second group of tests, we fix the final integration time at $t_f = 0.2$ and the element order at 18, and vary the time step size systematically between $\Delta t = 1.220703125 \times 10^{-5}$ and $\Delta t = 0.0125$. Fig. 1(c) shows the L^2 errors of the flow variables as a function of Δt in logarithmic scales. These results again correspond to the outflow condition OBC-E. On can observe a second-order convergence rate in time for the flow variables as Δt becomes small.

We next briefly compare the results from the pressure correction and velocity correction schemes. In [14] the outflow condition OBC-E given by Eq. (9) is proposed, and a velocity correction-type scheme has been developed for numerically treating this boundary condition. By contrast, the scheme in the current paper is based on a pressure correction-type strategy. Fig. 2 shows the L^2 errors of the y velocity component v and the pressure p as a function of the element order obtained with the current pressure correction scheme and the velocity correction scheme from [14], together with the OBC-E condition on the outflow boundary. The time step size and the final integration time are fixed at $\Delta t = 0.001$ and $t_f = 0.1$ in these tests, respectively. We can observe certain differences in the behaviors of these two schemes. The velocity errors from the two schemes are comparable. At large element orders (beyond 10) the velocity error from the pressure correction scheme is saturated at a level slightly lower than that from the velocity correction scheme. On the other hand, the errors for the pressure from the pressure correction scheme appear consistently larger than those from the velocity correction scheme. As the element order increases to 12 and beyond, the pressure error from the velocity correction scheme becomes saturated and the error curve levels off, while for the pressure correction scheme one can still observe a slight but noticeable decrease in the pressure error in this range.

3.1.2. Kovasznay flow

The goal of this subsection is to use a steady-state flow problem, the Kovasznay flow [45], to study the convergence behaviors of different outflow boundary conditions discussed in Section 2 and their effects on the flow field. This flow problem has been considered in [14] together with the OBC-E condition developed therein. Note that here we are testing a different numerical algorithm than that of [14] and different outflow boundary conditions. The problem parameters and configurations employed here largely follow those in [14].

Specifically, the velocity and the pressure of the Kovasznay flow are given by

$$\begin{cases} u = 1 - e^{\lambda x}\cos 2\pi y \\ v = \frac{\lambda}{2\pi} e^{\lambda x}\sin 2\pi y \\ p = \frac{1}{2}\left(1 - e^{2\lambda x}\right) \end{cases} \tag{44}$$

where $\lambda = -\frac{1}{2\nu}\left(\sqrt{1+16\pi^2\nu^2} - 1\right)$ is a parameter. The non-dimensional viscosity is fixed at $\nu = \frac{1}{40}$ for this test problem. In Eq. (2a), the body force is set to $\mathbf{f} = 0$ for this problem.

We consider a flow domain in accordance with [14], $-0.5 \leqslant x \leqslant L$ and $-0.5 \leqslant y \leqslant 0.5$, where either $L = -0.1$ or $L = 5.0$ for this problem. Fig. 3(a) is a sketch of the streamlines on the smaller domain with $L = -0.1$.

We focus on the domain with $L = -0.1$. To simulate the problem, we discretize the domain using two equal-sized quadrilateral spectral elements along the y direction. The element order is varied systematically in the tests. Periodic boundary conditions are imposed on the top/bottom sides of the domain ($y = \pm 0.5$). On the left side of domain ($x = -0.5$) we impose the Dirichlet condition for the velocity according to the expressions given in (44). On the right side of domain ($x = L$) we impose the outflow boundary condition (17), where $\mathbf{f}_b$ is chosen such that the velocity and the pressure as given in (44) ... $= L$. We employ a zero initial velocity, i.e. $\mathbf{u}_{in} = 0$ in (16), in the simulations. Table 2 lists the ...

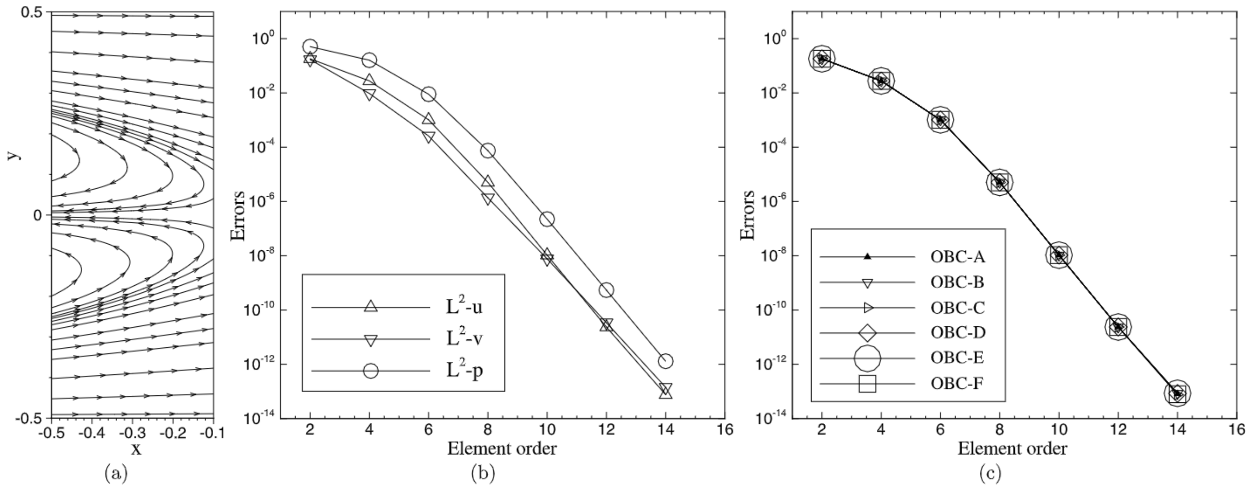

Fig. 3. Kovasznay flow on domain $L = -0.1$: (a) Streamlines. (b) L^2 errors as a function of element order, computed with OBC-C or $(\theta, \alpha_1, \alpha_2) = (1, 1, 0)$ outflow condition. (c) L^2 errors of the x velocity component as a function of element order, computed with different outflow boundary conditions.

Table 2
Kovasznay flow: physical and numerical parameters.

Parameter	Value	Parameter	Value
ν	0.025	Δt	0.001
L	−0.1, 5.0	U_0	1.0
J (temporal order)	2	δ	0.05

We vary the element order systematically between 2 and 14. For each element order we march in time using the algorithm discussed in Section 2 until the flow reaches a steady state. Then we compute the errors of the steady-state numerical solution against the exact expressions given by (44).

Let us look into the convergence behaviors. Fig. 3(b) shows the errors of the velocity and the pressure in L^2 norm as a function of the element order obtained using the OBC-C condition, i.e. $(\theta, \alpha_1, \alpha_2) = (1, 1, 0)$, on the right domain boundary $x = L$. It clearly shows an exponential convergence rate. Fig. 3(c) shows the L^2 errors of the x velocity component u as a function of the element order obtained using the different outflow conditions OBC-A to OBC-F on the right domain boundary. The different error curves essentially overlap with one another, indicative of an exponential convergence rate with all these outflow conditions.

Let us now consider another group of tests similar to that performed in [14]. In these tests we set $\mathbf{f}_b = 0$ in the outflow condition (17) to mimic real flows where the true $\mathbf{f}_b$ is unknown. Because of this error on the outflow boundary, as the resolution increases, the total error of the numerical solution will eventually be dominated and saturated by this factor. Fig. 4(a) demonstrates this behavior with the L^2 errors of the flow variables using the OBC-C outflow condition on the domain $L = -0.1$. Note that when computing the pressure errors we have used the shifted pressure $p = \frac{1}{2}\left(1 - e^{2\lambda x}\right) - \frac{1}{2}\left(1 - e^{2\lambda L}\right)$, as explained in [14]. It can be observed that as the element order increases, after the initial exponential decrease, the errors rapidly saturate as the element order reaches 6 and above.

Fig. 4(b) compares the L^2 errors of the x velocity component obtained using different outflow conditions at the right boundary. The same convergence behavior is observed with the various outflow boundary conditions. Some difference in the error magnitudes can be observed with different outflow conditions, especially upon saturation. But overall the difference is very small.

This observation is reinforced by the results obtained with $\mathbf{f}_b = 0$ on a larger domain corresponding to $L = 5.0$ as shown in Fig. 5. This figure shows the L^2 errors of different flow variables obtained using the OBC-C outflow condition (Fig. 5(a)) and the L^2 errors of the x velocity component corresponding to different outflow conditions (Fig. 5(b)). The larger domain ($-0.5 \leqslant x \leqslant 5.0$ and $-0.5 \leqslant y \leqslant 0.5$) has been partitioned using 6 quadrilateral spectral elements, with 2 uniform elements in the y direction and 3 non-uniform elements in the x direction (interior element boundaries located at $x = 0$ and 0.5). Fig. 5 demonstrates a similar behavior to that observed on the smaller domain. However, the error level at saturation is significantly lower than that for the smaller domain.

3.2. Flow past a circular cylinder

...r the canonical flow past a circular cylinder in a range of Reynolds numbers. In particular, ...lts obtained using our method with the experimental measurements and also with other

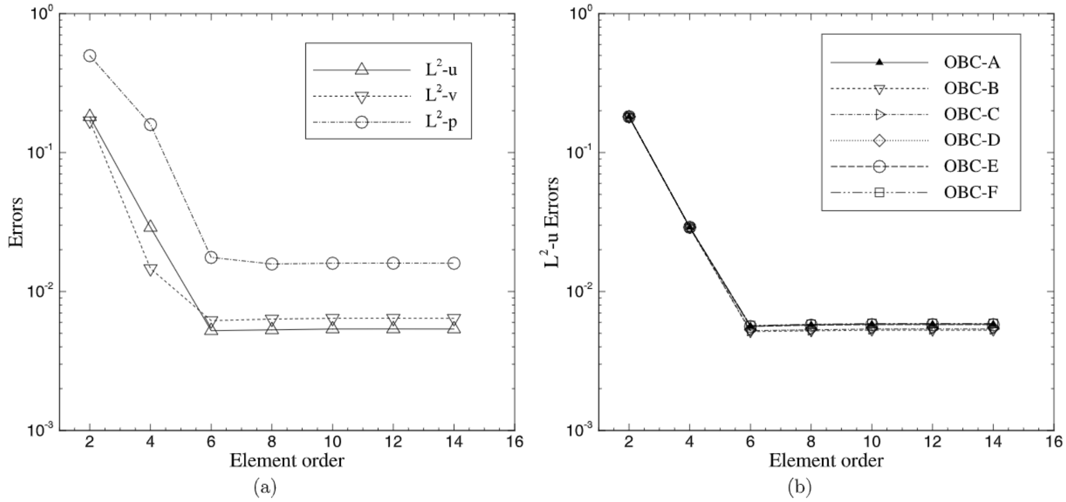

Fig. 4. Kovasznay flow on domain $L = -0.1$ computed with $\mathbf{f}_b = 0$ in outflow boundary condition: (a) L^2 errors vs. element order, computed using the OBC-C outflow condition. (b) L^2 errors of the x velocity component vs. element order, computed using different outflow boundary conditions.

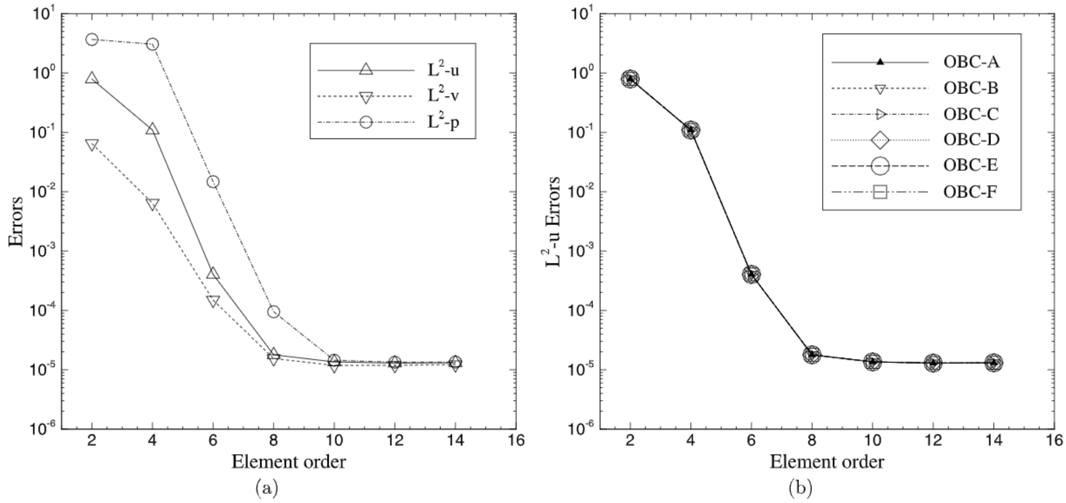

Fig. 5. Kovasznay flow on domain $L = 5.0$ computed with $\mathbf{f}_b = 0$ in outflow boundary condition: (a) L^2 errors vs. element order, computed using the OBC-C outflow condition. (b) L^2 errors of the x velocity component vs. element order, computed using different outflow boundary conditions.

simulations from the literature. We also demonstrate the stability of our algorithm at high Reynolds numbers when strong vortices or backflows occur at the outflow boundaries.

The problem setting is as follows. Consider a circular cylinder (or disk) of diameter D, and the flow around the cylinder in a rectangular domain (see Fig. 6), $-5D \leqslant x \leqslant L$ and $-10D \leqslant y \leqslant 10D$, where L is the length of the wake region to be specified subsequently. A uniform inflow, with a velocity along the horizontal direction and of unit magnitude, enters the domain through the left boundary ($x = -5D$). The flow leaves the domain on the right side ($x = L$). On the top and bottom sides of the domain we assume that the flow is periodic. So the configuration in practice corresponds to the flow past an array of circular cylinders.

We have considered four domain sizes corresponding to $L = 5D$, $10D$, $15D$ and $20D$ (Fig. 6). The majority of simulations are performed on the domain with $L = 10D$, and simulations on the other domains have also been conducted at several selected Reynolds numbers. We define the Reynolds number as

$$Re = \frac{1}{\nu} = \frac{U_0 D}{\nu_f} \tag{45}$$

where $U_0 = 1$ is the free-stream inflow velocity, ν_f is the kinematic viscosity of the fluid, and ν is the non-dimensional
The Reynolds numbers covered in the current simulations range from $Re = 20$ to $Re = 5000$.
alized by L, and all the velocity variables are normalized by U_0.

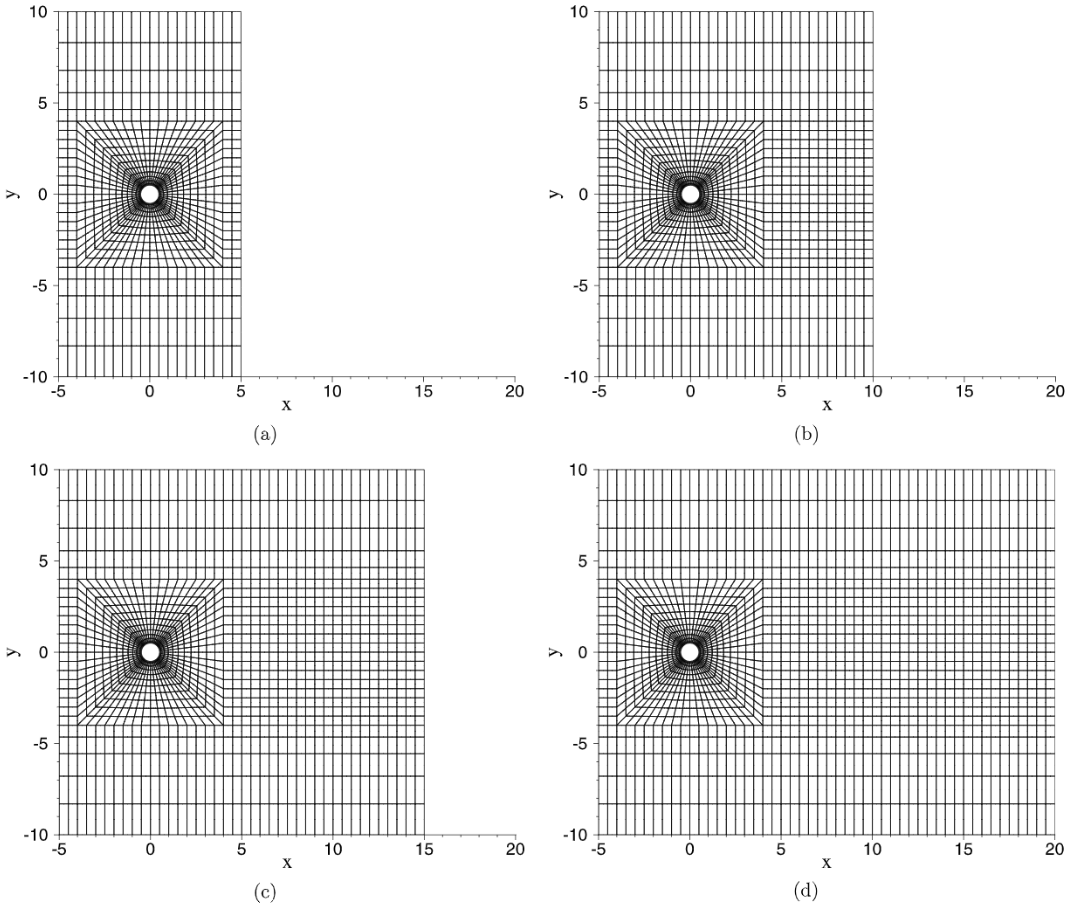

Fig. 6. Circular cylinder flow: Flow domains of different sizes and spectral-element meshes with (a) 968, (b) 1228, (c) 1488, and (d) 1748 quadrilateral elements.

The flow domains have been discretized using several spectral element meshes. Corresponding to the four domain sizes, the meshes respectively consist of 968, 1228, 1488 and 1748 quadrilateral elements; see Fig. 6. On the left domain boundary we impose the Dirichlet condition (3), where the boundary velocity is set to $\mathbf{w} = (U_0, 0)$. On the top and bottom boundaries ($y/D = \pm 10$) the periodic condition is imposed. On the right boundary ($x = L$) we impose the open boundary condition (17) with $\mathbf{f}_b = 0$ and $\delta = 0.01$.

We employ the algorithm developed in Section 2 for marching in time. An element order 6 has been used for each element at low Reynolds numbers (below $Re = 100$), and order 8 has been used for each element for higher Reynolds numbers. We have monitored the forces on the cylinder. The numerical experiments indicate that the drag and lift coefficients essentially do not change any more or only change slightly when we increase the element order further. We use a time step size $\Delta t = 10^{-3}$ for Reynolds numbers below 100, and $\Delta t = 2.5 \times 10^{-4}$ for higher Reynolds numbers.

The general features of the circular cylinder flow at Reynolds numbers of various flow regimes have been discussed in detail in [77]. At Reynolds number around $Re = 47$ the cylinder wake experiences an instability, and it becomes unsteady with vortex shedding from the cylinder. The flow is two-dimensional at this point. When the Reynolds number increases to around $Re = 180$, another instability develops in the cylinder wake, and the physical flow becomes three-dimensional. In Fig. 7 we show contours of the instantaneous vorticity from our simulations at three Reynolds numbers $Re = 20$ (plot (a)), 100 (plot (b)), and 300 (plot (c)). These results correspond to the domain size $L = 10D$ and the outflow condition OBC-E, i.e. $(\theta, \alpha_1, \alpha_2) = (1, 0, 0)$ in (17). Fig. 7(a) corresponds to a steady-state flow, while Fig. 7(b) and (c) show vortex shedding at the higher Reynolds numbers. These are two-dimensional simulations. In reality, the physical flow at $Re = 300$ has already become three-dimensional.

We have monitored the signals of the forces acting on the cylinder. Fig. 8 shows time histories of the lift, i.e. the y component of the force, at Reynolds numbers $Re = 100$ (Fig. 8(a)) and $Re = 1000$ (Fig. 8(b)). These results are obtained on the domain $L = 10D$ using the OBC-E outflow condition on the right boundary. One can observe that the lift force fluctuates egular fashion at these Reynolds numbers, while the amplitude and frequency of these signals

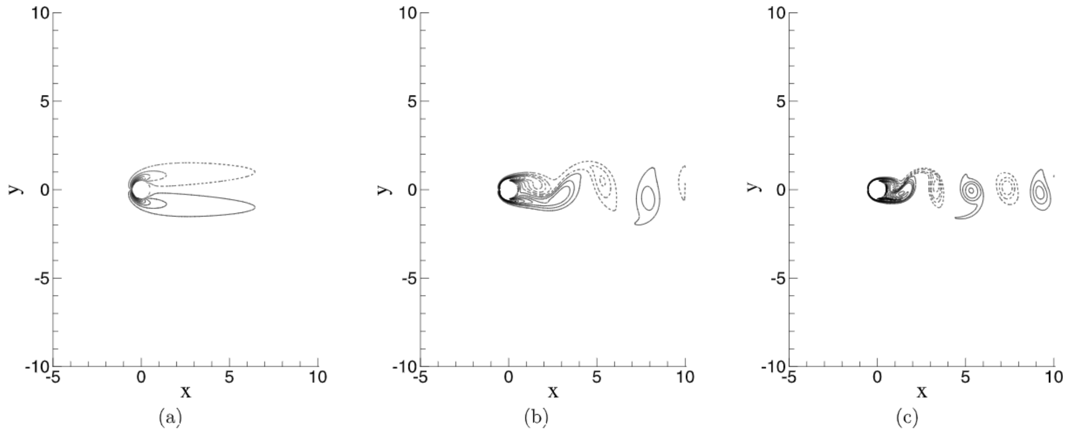

Fig. 7. Circular cylinder flow: Contours of instantaneous vorticity at Reynolds numbers (a) $Re = 20$, (b) $Re = 100$, and (c) $Re = 300$. Dashed curves denote negative vorticity values.

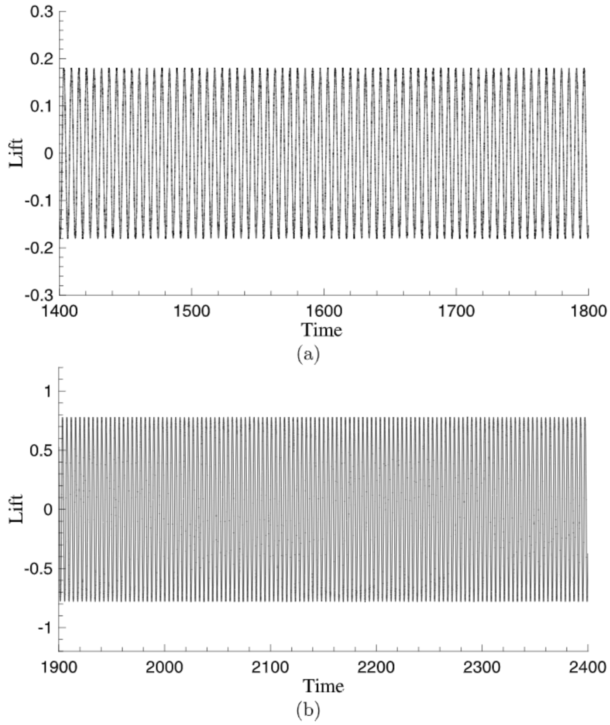

Fig. 8. Circular cylinder flow: Time histories of the lift force on the cylinder at Reynolds numbers (a) $Re = 100$ and (b) $Re = 1000$.

We have computed the mean drag coefficient (C_d) and the root-mean-square (RMS) lift coefficient (C_L) on the cylinder from the simulations. These coefficients are respectively defined as

$$C_d = \frac{\overline{F}_x}{\frac{1}{2}\rho U_0^2}, \qquad C_L = \frac{F'_y}{\frac{1}{2}\rho U_0^2}, \tag{46}$$

where $\overline{F}_x$ is the mean (time-averaged) drag, i.e. the x component of force, on the cylinder, F'_y is the RMS of the lift, and ρ is the fluid density. In Fig. 9(a) we compare the mean drag coefficient as a function of the Reynolds number between current simulations and the experimental measurements of [76,11,19,74,67]. The drag coefficients from the three-dimensional simulations of [52,13] are also shown in the figure. The results of the current simulations are obtained using the OBC-E (i.e. $(\theta, \alpha_1, \alpha_2) = (1, 0, 0)$) open boundary condition. The majority are for the flow domain $L = 10D$, while at $Re = 20$ and $Re = 100$ results are also obtained using the domains $L = 5D$ and $L = 20D$ for this group of tests. Note also that the cur-
e can observe that, in the 2-D regime the drag coefficients from current simulations are in
ental data. In the 3-D regime, i.e. at Reynolds numbers beyond about $Re = 180$ when the

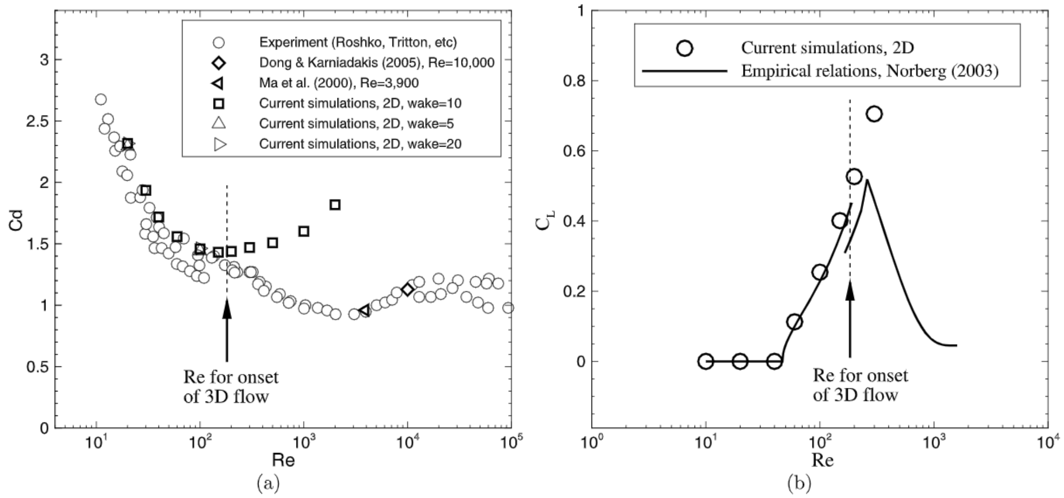

Fig. 9. Circular cylinder flow: Comparisons of (a) drag coefficients and (b) RMS lift coefficients as a function of the Reynolds number between current simulations and experimental measurements. Results of current simulations correspond to the OBC-E outflow condition, i.e. $(\theta, \alpha_1, \alpha_2) = (1, 0, 0)$.

Table 3
Circular cylinder flow: Comparison of RMS lift coefficients at $Re = 100$ and $Re = 200$ between current simulations and existing simulations from literature.

Source	$Re = 100$	$Re = 200$
Braza et al. (1986) [6]	0.21	0.55
Karniadakis (1988) [40]	–	0.48
Engelman and Jamnia (1990) [17]	0.26	–
Meneghini and Bearman (1993) [53]	–	0.54
Beaudan and Moin (1994) [3]	0.24	–
Zhang et al. (1995) [78]	0.25	0.53
Newman and Karniadakis (1995) [55]	–	0.51
Tang and Audry (1997) [71]	0.21	0.45
Persillon and Braza (1998) [63]	0.27	0.56
Zhang and Dalton (1998) [79]	–	0.48
Kravchenko et al. (1999) [46]	0.22	–
Hwang and Lin (1992) [36]	0.27	0.42
Newman and Karniadakis (1996) [56]	0.24	–
Dong and Shen (2010) [16]	–	0.501
Franke et al. (1990) [22]	–	0.46
Current simulations (wake = 5)	0.261	–
Current simulations (wake = 10)	0.254	0.527
Current simulations (wake = 15)	0.253	–
Current simulations (wake = 20)	0.253	–

physical flow of the wake becomes three-dimensional, one can observe a marked discrepancy between the drag coefficients from the current 2-D simulations and the experimental data. This discrepancy becomes more pronounced with increasing Reynolds number.

Fig. 9(b) shows a comparison of the RMS lift coefficient as a function of the Reynolds number between the current simulations and the empirical relation given by Norberg [57]. The simulation results are obtained on the domain $L = 10D$ with the OBC-E open boundary condition. In the 2-D regime, the RMS lift results from current simulations agree with the empirical relation reasonably well. However, at Reynolds numbers in the 3-D regime, the current simulations significantly over-predict the lift coefficient, which is a well-known issue with 2-D simulations [13,15].

In Table 3 we list the RMS lift coefficients at $Re = 100$ and $Re = 200$ from current simulations. At $Re = 100$ the lift coefficients have been obtained on four domains $L = 5D$, $10D$, $15D$ and $20D$, while at $Re = 200$ the result is for the domain $L = 10D$. For comparison, we have also listed in this table the lift coefficients from existing simulations from the literature for these two Reynolds numbers. First, one can observe that the domain size (or the size of the wake region) has a certain effect on the lift coefficient. As the wake region increases to a certain size, e.g. about $L = 10D$ at $Re = 100$, the obtained lift coefficient essentially will not change any longer or only change very slightly. Second, the lift coefficients from the existing simulations in the literature exhibit a spread over a range of values. The results from current simulations appear in good agreement with the existing simulation data, and lie well within the range of existing data.

bility issue with the outflow boundaries at higher Reynolds numbers. As the Reynolds number
from the cylinder can persist a long time in the wake before being sufficiently dissipated.

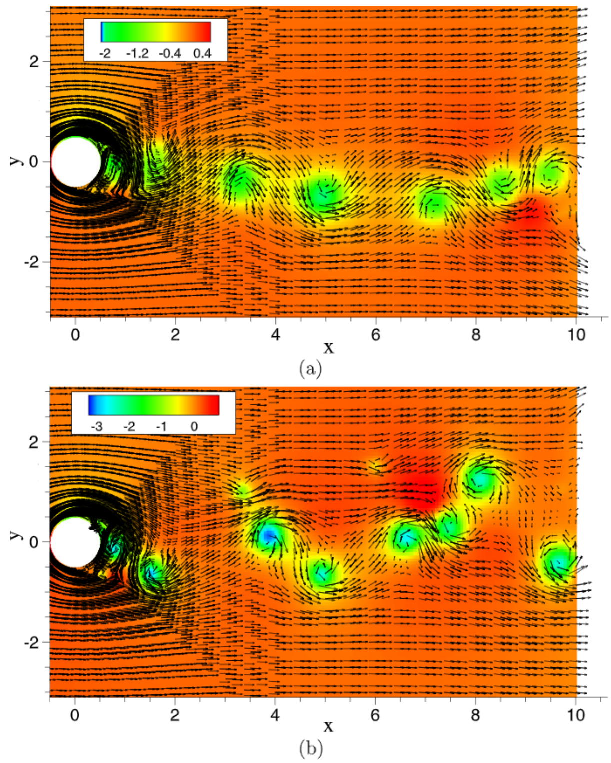

Fig. 10. (Color online.) Instantaneous velocity fields and pressure distributions (color contours) of cylinder flow: (a) $Re = 2000$, corresponding to the OBC-E outflow condition or $(\theta, \alpha_1, \alpha_2) = (1, 0, 0)$, (b) $Re = 5000$, corresponding to the OBC-C outflow condition or $(\theta, \alpha_1, \alpha_2) = (1, 1, 0)$. Velocity vectors are plotted on every fifth quadrature point in each direction within each element.

For a given computational domain with a certain size for the wake region, as the Reynolds number becomes sufficiently large, the strong vortices shed from the cylinder will eventually reach the outflow/open boundary. These vortices can induce backflows at the open boundaries, and with usual outflow/open boundary conditions the simulations will instantly become unstable. This is a well-known numerical instability associated with the open boundaries.

The open boundary conditions we presented in Section 2 are effective in dealing with this instability, because these conditions ensure the energy stability of the system even in the presence of strong vortices or backflows at the open boundaries. Fig. 10 shows the instantaneous velocity fields and the pressure distributions (color contours) at Reynolds numbers $Re = 2000$ and $Re = 5000$. They are obtained with the domain size $L = 10D$. The results for $Re = 2000$ and $Re = 5000$ respectively correspond to the OBC-E and OBC-C conditions at the open boundary. One can clearly observe the strong vortices at the open boundary at these Reynolds numbers. The current open boundary conditions and the pressure correction-based algorithm produce stable simulations in these situations. On the other hand, we observe that with the traction-free boundary condition (see e.g. [69]) or its variant the no-flux boundary condition (i.e. $\frac{\partial \mathbf{u}}{\partial n} = 0$ and $p = 0$) the computation blows up instantly when the vortices hit the open boundary at these Reynolds numbers. We have performed very long-time simulations of the cylinder flow with the open boundary conditions and the algorithm developed herein. Fig. 11 shows a window of the time histories of the drag force on the cylinder at $Re = 5000$ obtained with different open boundary conditions. These force histories demonstrate the long-time stability of our method.

Let us next consider the effect of different open boundary conditions on the results. We observe that the results obtained using the several open boundary conditions from Section 2.1 are quite similar. The two drag histories in Fig. 11 for $Re = 5000$ are obtained respectively with the OBC-E and OBC-C open boundary conditions. Their characteristics appear qualitatively similar to each other. In Table 4 we have listed the mean drag coefficient Cd, RMS drag coefficient Cd_{rms}, and the RMS lift coefficient C_L at $Re = 5000$ obtained with the several open boundary conditions in Section 2.1. The RMS drag coefficient is defined as $Cd_{rms} = \frac{F_x'}{\frac{1}{2}\rho U_0^2}$, where F_x' is the RMS of the drag. One can observe that these force coefficients are quantitatively very close, with the maximum difference on the order of $2 \sim 3\%$.

Finally let us take a look at the discharge of vortices away from the domain through the open boundary and the effects of different open boundary conditions. We observe that with these open boundary conditions the vortices can cross the open boundary in a generally natural way, and that a certain amount of distortion to the vortices occurs during this process. This is illustrated in Fig. 12 by a temporal sequence of snapshots of the velocity fields at $Re = 2000$ computed using the C on a domain with $L = 10D$. This figure shows how the vortex initially located above the ht boundary in Fig. 12(a) is discharged through the outflow boundary. As the vortex core

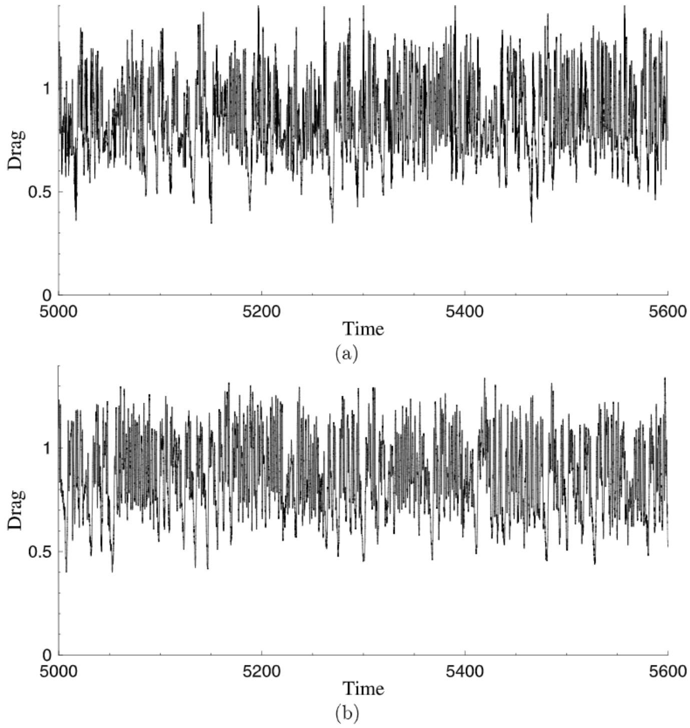

Fig. 11. Cylinder flow at $Re = 5000$: Time histories of drag obtained with different outflow boundary conditions corresponding to (a) OBC-E condition or $(\theta, \alpha_1, \alpha_2) = (1, 0, 0)$ and (b) OBC-C condition or $(\theta, \alpha_1, \alpha_2) = (1, 1, 0)$.

Table 4
Circular cylinder flow at $Re = 5000$: Comparison of the mean drag coefficient C_d, RMS drag coefficient Cd_{rms} and RMS lift coefficient C_L obtained with different outflow boundary conditions corresponding to different parameters $(\theta, \alpha_1, \alpha_2)$.

$(\theta, \alpha_1, \alpha_2)$ or type	Cd	Cd_{rms}	C_L
$(\frac{1}{2}, 0, 0)$ or OBC-A	1.743	0.377	1.440
$(1, 0, 1)$ or OBC-B	1.738	0.386	1.434
$(1, 1, 0)$ or OBC-C	1.738	0.378	1.428
$(0, 1, 0)$ or OBC-D	1.736	0.379	1.423
$(1, 0, 0)$ or OBC-E	1.726	0.380	1.420
$(0, 0, 0)$ or OBC-F	1.699	0.373	1.403

passes through the open boundary (Fig. 12(d)–(f)), one can observe a distortion in the velocity patterns, and the vortex does not quite appear "circular" any more (see Fig. 12(e)). This distortion to the vortices has also been observed with the other open boundary conditions considered here. In addition, when the vortices cross the open boundary, we have observed that the individual $(\mathbf{n} \cdot \mathbf{u})\mathbf{u}$ term in the open boundary condition (as in OBC-D and OBC-F) tends to have the effect of somewhat causing the vortices to move sideways along the open boundary, and that the individual $|\mathbf{u}|^2\mathbf{n}$ term (as in OBC-B and OBC-E) tends to have the effect of somewhat squeezing the vortices along the direction normal to the open boundary. The conditions OBC-C and OBC-A are combinations of these two terms, and the two individual effects seem to fade and largely invisible when these open boundary conditions are used. It is also observed that the current method for treating the outflows is subject to the usual constraints of spatial and temporal resolutions. For example, if the mesh resolution is too low at the open boundary and when the vortices pass through, the velocity field computed from the current algorithm and open boundary conditions may exhibit characteristics of under-resolved flows at the open boundary near the vortex cores. The boundary condition OBC-E appears somewhat more sensitive to this resolution effect compared to the other open boundary conditions considered here.

3.3. Impinging jet on a wall with open boundaries

In this section we consider a jet impinging on a solid wall involving open domain boundaries in two dimensions. At [illegible]umbers, the instability of the jet and the presence of the open boundaries make this problem

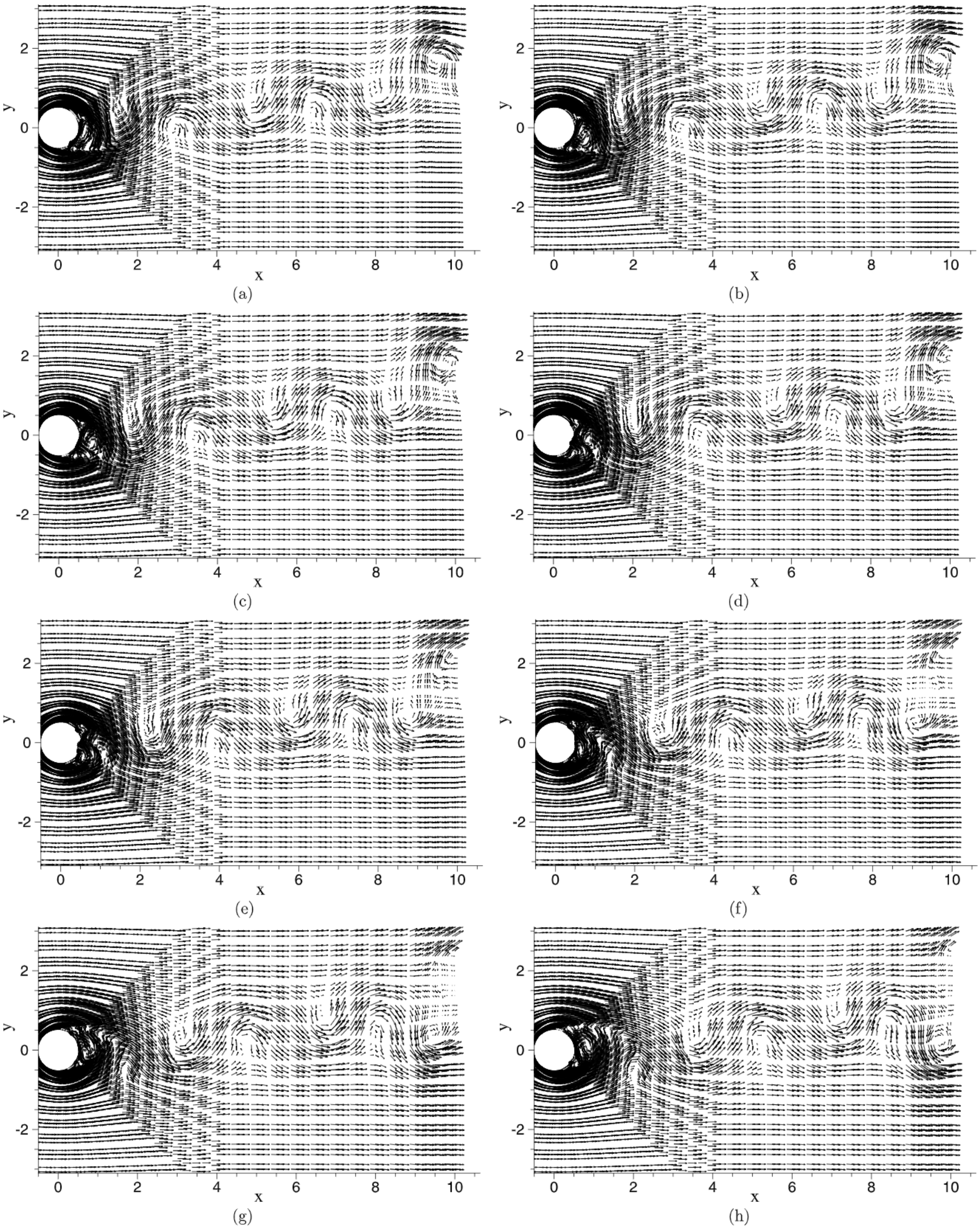

Fig. 12. Temporal sequence of snapshots of velocity fields at $Re = 2000$ showing the discharge of vortices away from the domain, computed using the outflow boundary condition OBC-C. (a) $t = 438.5$, (b) $t = 438.75$, (c) $t = 439$, (d) $t = 439.25$, (e) $t = 439.5$, (f) $t = 440$, (g) $t = 440.5$, (h) $t = 441$. Velocity vectors are plotted on every fifth quadrature point in each direction within each element.

We refer to Fig. 13 for the configuration of this problem. Consider a fluid jet, of diameter D, issuing into a rectangular ... The domain has the following dimension, $-\frac{5}{2}D \leqslant x \leqslant \frac{5}{2}D$ and $0 \leqslant y \leqslant 5D$. The top and bottom ... ile the left and right sides of the domain are open, where the fluid can leave or enter the

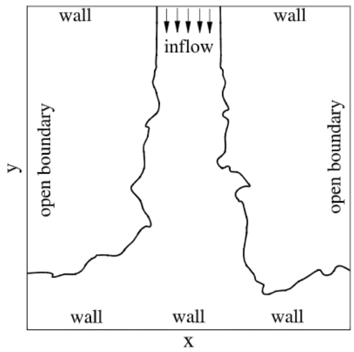

Fig. 13. Flow configuration for the impinging jet on a wall with open boundaries.

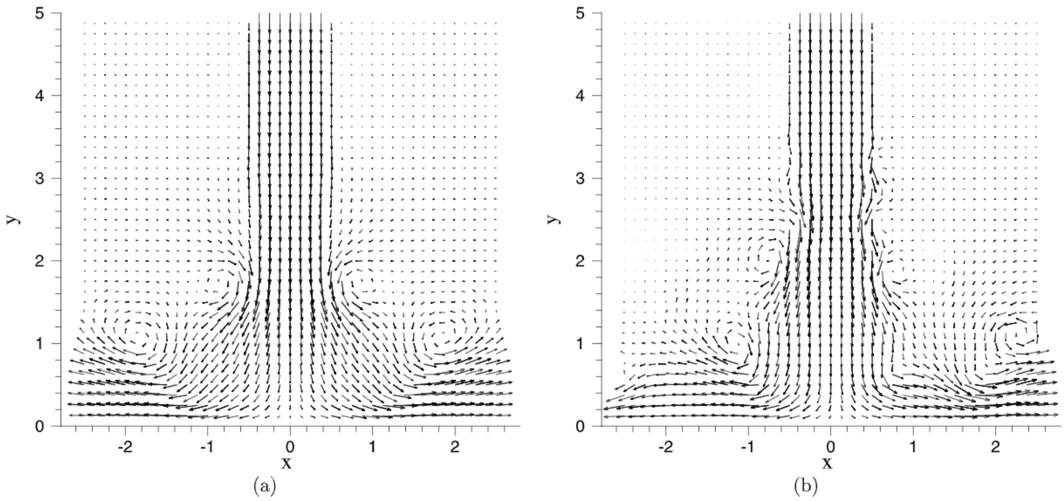

Fig. 14. Impinging jet on a wall: Instantaneous velocity distributions at Reynolds numbers (a) $Re = 2000$ and (b) $Re = 5000$, obtained using the OBC-C open boundary condition or $(\alpha, \alpha_1, \alpha_2) = (1, 1, 0)$. Velocity vectors are plotted on every eleventh quadrature point in each direction within each element.

domain freely. The center of the jet is aligned with the middle of the top wall. We assume that at the inlet the jet velocity is along the vertical direction and has the following profile,

$$\begin{cases} u = 0 \\ v = -U_0 \left[\tanh \dfrac{1 - \frac{x}{R_0}}{\sqrt{2}\epsilon} \left[H(x, 0) - H(x, R_0) \right] + \tanh \dfrac{1 + \frac{x}{R_0}}{\sqrt{2}\epsilon} \left[H(x, -R_0) - H(x, 0) \right] \right] \end{cases} \tag{47}$$

where $U_0 = 1$ is a velocity scale, $R_0 = \frac{D}{2}$ is the jet radius, and $\epsilon = \frac{1}{40} D$. $H(x, x_0)$ is the Heaviside step function, taking unit value if $x \geqslant x_0$ and vanishing otherwise.

All the length variables are normalized by the jet diameter D, and all velocities are normalized by U_0. The Reynolds number for this problem is defined by Eq. (45), noting the specific physical meanings of U_0 and D for this problem. We assume that there is no external body force.

The domain has been discretized using 400 quadrilateral elements of equal sizes, with 20 elements in both the x and y directions. We impose the velocity Dirichlet boundary condition (3) on the top and bottom sides of the domain, where the boundary velocity is set to $\mathbf{w} = 0$ at the walls and set according to Eq. (47) at the jet inlet. On the left and right sides of the domain the open boundary condition (17) is imposed, with $\mathbf{f}_b = 0$ and $\delta = \frac{1}{100}$. Different $(\theta, \alpha_1, \alpha_2)$ parameters have been tested corresponding to the open boundary conditions OBC-A to OBC-F.

We employ the algorithm developed in Section 2 in the simulations, and have considered several Reynolds numbers ranging from $Re = 2000$ to $Re = 10\,000$. The element order in the simulations ranges from 12 for $Re = 2000$ to 16 for $Re = 10\,000$. The time step size ranges from $\frac{U_0 \Delta t}{D} = 2.5 \times 10^{-4}$ for $Re = 2000$ to $\frac{U_0 \Delta t}{D} = 2 \times 10^{-4}$ for $Re = 10\,000$.

We first look into the basic features of this flow. Fig. 14(a) shows the instantaneous velocity distribution at $Re = 2000$. The jet profile appears to be stable within a certain distance downstream of the inlet, $2 \lesssim y/D \leqslant 5$ in this case. Beyond this ortices to form along the profile of the jet. After impinging onto the bottom wall the jet splits t of the domain respectively through the left and the right open boundaries. The vortices

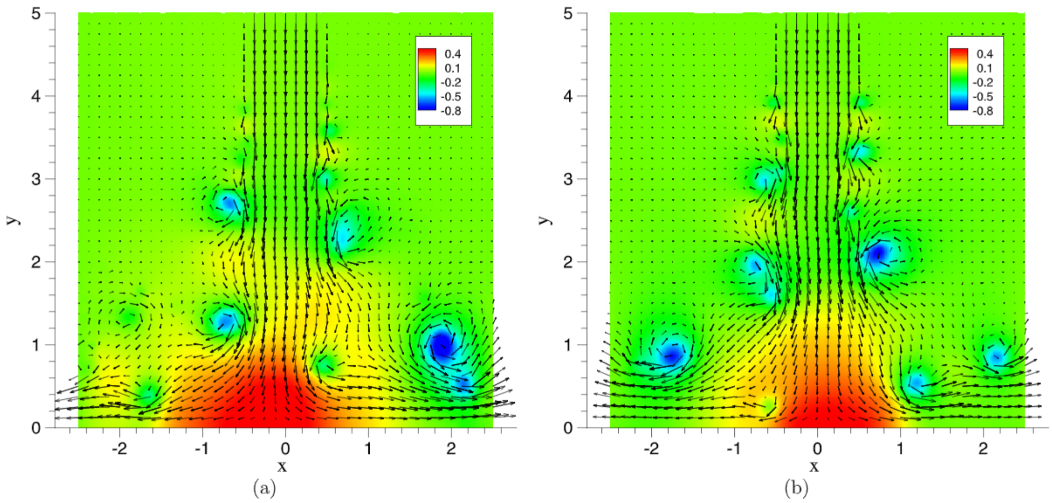

Fig. 15. (Color online.) Impinging jet on a wall: Instantaneous velocity fields, and pressure distributions (color contours), at $Re = 10\,000$ obtained using open boundary conditions (a) OBC-A, or $(\theta, \alpha_1, \alpha_2) = (\frac{1}{2}, 0, 0)$ and (b) OBC-B, or $(\theta, \alpha_1, \alpha_2) = (1, 0, 1)$. Velocity vectors are plotted on every eleventh quadrature point in each direction within each element.

formed on the edges of the jet are convected out of domain alongside the horizontal streams. The velocity distribution appears to be symmetric about the jet centerline ($x = 0$) at this Reynolds number.

Fig. 14(b) shows the distribution of the instantaneous velocity at a higher Reynolds number $Re = 5000$. One can observe a basic feature similar to that of $Re = 2000$. However, the region with a stable jet profile downstream of the inlet is smaller, with $3.5 \lesssim y/D \leqslant 5$ at $Re = 5000$. In addition, the velocity distribution has lost the symmetry about the jet centerline.

The vortices formed along the jet profile cause the backflow instability on the left and right open boundaries, and pose a severe challenge to the simulation of this problem. The open boundary conditions and the numerical algorithm developed in Section 2 are crucial to the stability of the simulations. In contrast, usual open boundary conditions such as the traction-free condition and the no-flux condition are unstable for the Reynolds numbers simulated here, and we observe that the computation blows up instantly when the vortices hit the open boundaries.

Let us next look into the effect of different open boundary conditions on the flow characteristics and the physical quantities. In Fig. 15 we show the instantaneous velocity fields and the pressure distributions at $Re = 10\,000$ obtained using the OBC-A and OBC-B open boundary conditions. The characteristics of the flow obtained with these boundary conditions are qualitatively similar. One can observe that the jet profile develops an instability at an even shorter distance downstream of the inlet (around $y/D = 4$) than at the lower Reynolds numbers (Fig. 14). The vortices in the flow also appear more populous.

We have performed long-time simulations of this flow using different open boundary conditions. Fig. 16 shows a window of the time histories of the vertical force component (F_y) on the walls at $Re = 10\,000$ obtained with the OBC-C and OBC-D open boundary conditions. Note that the horizontal component of the force is essentially zero. One can observe the chaotic fluctuations of the force signals about some mean value. The characteristics of the force histories appear to be qualitatively similar. A quantitative comparison is shown in Table 5, where we have listed the time-averaged mean and the RMS forces (vertical component) on the wall obtained using the several open boundary conditions from Section 2.1. The mean forces corresponding to different boundary conditions are very close, with the maximum difference among them about 4%. The RMS forces obtained with different open boundary conditions are also comparable. While the RMS forces with the other open boundary conditions are quite close, those corresponding to OBC-E and OBC-B are somewhat smaller.

4. A provably unconditionally stable scheme for a sub-class of open boundary conditions

In this section we briefly discuss a rotational pressure correction scheme with a provable unconditional stability for the following sub-class of the open boundary conditions (11),

$$\theta = \alpha_2 = 0, \quad \alpha_1 \geqslant 0. \tag{48}$$

The boundary conditions OBC-D and OBC-F belong to this sub-class.

Our discussions here will be limited to the temporal discretization only, and it is assumed that the field variables are continuous in space in this section. The stability proof is provided for the scheme with a nominal first order in time. We assume a homogeneous velocity Dirichlet condition on $\partial\Omega_d$, i.e. $\mathbf{w} = 0$ in (3), and that there is no external body force, i.e. ssume that $\mathbf{f}_b = 0$ in the open boundary condition (11), and that $\delta \to 0$ in the $\Theta_0(\mathbf{n}, \mathbf{u})$

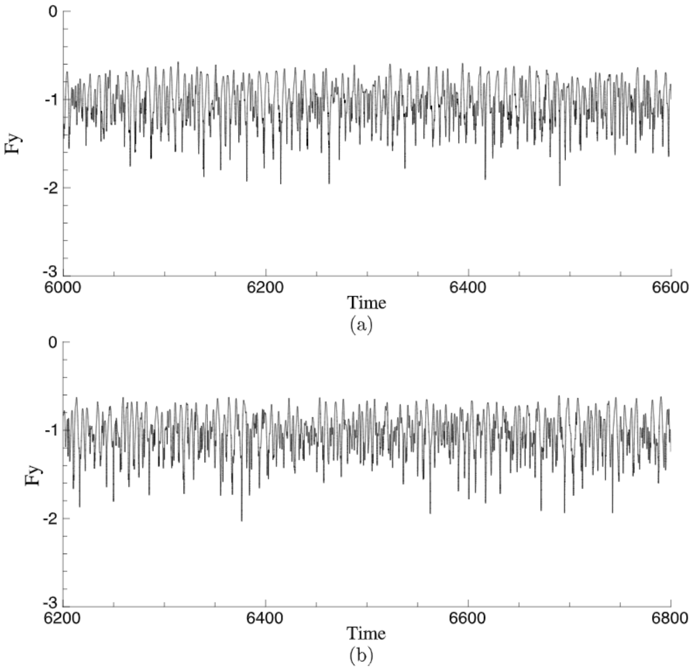

Fig. 16. Impinging jet on a wall at $Re = 10\,000$: Time histories of the force (vertical component) on the wall obtained using open boundary conditions (a) OBC-C, or $(\theta, \alpha_1, \alpha_2) = (1, 1, 0)$ and (b) OBC-D, or $(\theta, \alpha_1, \alpha_2) = (0, 1, 0)$.

Table 5
Impinging jet on a wall at $Re = 10\,000$: Mean and RMS forces (vertical component) on the wall obtained using different open boundary conditions.

$(\theta, \alpha_1, \alpha_2)$ or type	Mean F_y	RMS F_y
$(\frac{1}{2}, 0, 0)$ or OBC-A	−1.015	0.241
$(1, 0, 1)$ or OBC-B	−1.005	0.181
$(1, 1, 0)$ or OBC-C	−1.009	0.220
$(0, 1, 0)$ or OBC-D	−1.016	0.231
$(1, 0, 0)$ or OBC-E	−0.984	0.156
$(0, 0, 0)$ or OBC-F	−1.024	0.258

$$\lim_{\delta \to 0} \Theta_0(\mathbf{n}, \mathbf{u}) = \Theta_{s0}(\mathbf{n}, \mathbf{u}) = \begin{cases} 1, & \text{if } \mathbf{n} \cdot \mathbf{u} < 0, \\ 0, & \text{otherwise.} \end{cases} \tag{49}$$

Given $(\tilde{\mathbf{u}}^n, \mathbf{u}^n, p^n)$, we compute these field variables at time step $(n+1)$ as follows. First, find $\tilde{\mathbf{u}}^{n+1}$ satisfying

$$\frac{\tilde{\mathbf{u}}^{n+1} - \mathbf{u}^{\mathbf{n}}}{\Delta t} + \mathbf{u}^{\mathbf{n}} \cdot \nabla \tilde{\mathbf{u}}^{n+1} + \nabla p^n - \nu \nabla^2 \tilde{\mathbf{u}}^{n+1} = 0, \tag{50a}$$

$$\tilde{\mathbf{u}}^{n+1} = 0, \qquad \text{on } \partial\Omega_d, \tag{50b}$$

$$-p^n \mathbf{n} + \nu \mathbf{n} \cdot \nabla \tilde{\mathbf{u}}^{n+1} - (1 + \alpha_1) \frac{1}{2} (\mathbf{u}^n \cdot \mathbf{n}) \tilde{\mathbf{u}}^{n+1} \Theta_{s0}(\mathbf{n}, \mathbf{u}^n) = 0, \qquad \text{on } \partial\Omega_o. \tag{50c}$$

Then, find $(\mathbf{u}^{n+1}, p^{n+1})$ satisfying

$$\frac{\mathbf{u}^{n+1} - \tilde{\mathbf{u}}^{n+1}}{\Delta t} + \nabla \left(p^{n+1} - p^n + \chi \nabla \cdot \tilde{\mathbf{u}}^{n+1} \right) = 0, \tag{51a}$$

$$\nabla \cdot \mathbf{u}^{n+1} = 0, \tag{51b}$$

$$\mathbf{n} \cdot \mathbf{u}^{n+1} = 0, \qquad \text{on } \partial\Omega_d, \tag{51c}$$

$$p^{n+1} - p^n + \chi \nabla \cdot \tilde{\mathbf{u}}^{n+1} = 0, \qquad \text{on } \partial\Omega_o, \tag{51d}$$

o be specified subsequently.

Note that Eqs. (51a)–(51d) are equivalent to the following,

$$\nabla^2\left(p^{n+1} - p^n + \chi\nabla\cdot\tilde{\mathbf{u}}^{n+1}\right) = \frac{\nabla\cdot\tilde{\mathbf{u}}^{n+1}}{\Delta t}, \tag{52a}$$

$$\frac{\partial}{\partial\mathbf{n}}(p^{n+1} - p^n + \chi\nabla\cdot\tilde{\mathbf{u}}^{n+1}) = 0 \quad \text{on } \partial\Omega_d; \qquad p^{n+1} - p^n + \chi\nabla\cdot\tilde{\mathbf{u}}^{n+1} = 0 \quad \text{on } \partial\Omega_o, \tag{52b}$$

and

$$\mathbf{u}^{n+1} = \tilde{\mathbf{u}}^{n+1} - \Delta t\nabla(p^{n+1} - p^n + \chi\nabla\cdot\tilde{\mathbf{u}}^{n+1}). \tag{53}$$

To prove the stability of the scheme given by (50a)–(51d), we define the auxiliary variables q^n and ψ^n by $q^0 = -p^0$, and

$$q^{n+1} = q^n + \chi\nabla\cdot\tilde{\mathbf{u}}^{n+1}, \quad \psi^{n+1} = p^{n+1} + q^{n+1}. \tag{54}$$

Then, Eqs. (51a) and (51d) can be written as:

$$\frac{\mathbf{u}^{n+1} - \tilde{\mathbf{u}}^{n+1}}{\Delta t} + \nabla\left(\psi^{n+1} - \psi^n\right) = 0, \tag{55}$$

$$\psi^{n+1} - \psi^n = 0, \qquad \text{on } \partial\Omega_o. \tag{56}$$

Note that $\psi^0 = p^0 + q^0 = 0$, and hence we have

$$\psi^n = 0, \quad \text{on } \partial\Omega_o, \tag{57}$$

for all n based on Eq. (56).

Let (f, g) denote the L^2 inner product between field variables $f(\mathbf{x}, t)$ and $g(\mathbf{x}, t)$, and define $\|f\|^2 = (f, f)$. Taking the L^2 inner product between (50a) and $2\Delta t\tilde{\mathbf{u}}^{n+1}$, and noticing that (since $\nabla\cdot\mathbf{u}^{\mathbf{n}} = 0$)

$$(\mathbf{u}^{\mathbf{n}}\cdot\nabla\tilde{\mathbf{u}}^{n+1}, \tilde{\mathbf{u}}^{n+1}) = \frac{1}{2}\int_{\partial\Omega_o}(\mathbf{u}^n\cdot\mathbf{n})|\tilde{\mathbf{u}}^{n+1}|^2,$$

we obtain

$$\begin{aligned}
&\|\tilde{\mathbf{u}}^{n+1}\|^2 - \|\mathbf{u}^n\|^2 + \|\tilde{\mathbf{u}}^{n+1} - \mathbf{u}^n\|^2 + 2\nu\Delta t\|\nabla\tilde{\mathbf{u}}^{n+1}\|^2 - 2\Delta t(p^n, \nabla\cdot\tilde{\mathbf{u}}^{n+1}) \\
&\quad = 2\Delta t\int_{\partial\Omega_o}(\nu\mathbf{n}\cdot\nabla\tilde{\mathbf{u}}^{n+1} - p^n\mathbf{n})\cdot\tilde{\mathbf{u}}^{n+1} - 2\Delta t(\mathbf{u}^{\mathbf{n}}\cdot\nabla\tilde{\mathbf{u}}^{n+1}, \tilde{\mathbf{u}}^{n+1}) \\
&\quad = 2\Delta t\int_{\partial\Omega_o}\left(\nu\mathbf{n}\cdot\nabla\tilde{\mathbf{u}}^{n+1} - p^n\mathbf{n} - \frac{1}{2}(\mathbf{u}^n\cdot\mathbf{n})\tilde{\mathbf{u}}^{n+1}\right)\cdot\tilde{\mathbf{u}}^{n+1} \\
&\quad = \Delta t\int_{\partial\Omega_o}\left[(\mathbf{u}^n\cdot\mathbf{n})|\tilde{\mathbf{u}}^{n+1}|^2\left(\Theta_{s0}(\mathbf{n}, \mathbf{u}^n) - 1\right) + \alpha_1(\mathbf{u}^n\cdot\mathbf{n})|\tilde{\mathbf{u}}^{n+1}|^2\Theta_{s0}(\mathbf{n}, \mathbf{u}^n)\right] \\
&\quad \leqslant 0,
\end{aligned} \tag{58}$$

where we have used integration by part, the divergence theorem, and Eq. (50c).

We deal with the term $-2\Delta t(p^n, \nabla\cdot\tilde{\mathbf{u}}^{n+1}) = -2\Delta t(\psi^n - q^n, \nabla\cdot\tilde{\mathbf{u}}^{n+1})$ as follows. Note that

$$\begin{aligned}
-2\Delta t(\psi^n, \nabla\cdot\tilde{\mathbf{u}}^{n+1}) &= 2\Delta t(\nabla\psi^n, \tilde{\mathbf{u}}^{n+1}) = 2\Delta t(\nabla\psi^n, \mathbf{u}^{n+1} + \Delta t\nabla(\psi^{n+1} - \psi^n)) \\
&= 2\Delta t^2(\nabla\psi^n, \nabla(\psi^{n+1} - \psi^n)) \\
&= \Delta t^2(\|\nabla\psi^{n+1}\|^2 - \|\nabla\psi^n\|^2 - \|\nabla(\psi^{n+1} - \psi^n)\|^2) \\
&= \Delta t^2(\|\nabla\psi^{n+1}\|^2 - \|\nabla\psi^n\|^2) - \|\mathbf{u}^{n+1} - \tilde{\mathbf{u}}^{n+1}\|^2,
\end{aligned} \tag{59}$$

where we have use (51b), (55), and (57). Note also that

$$\begin{aligned}
2\Delta t(q^n, \nabla\cdot\tilde{\mathbf{u}}^{n+1}) &= \frac{2\Delta t}{\chi}(q^n, q^{n+1} - q^n) \\
&= \frac{\Delta t}{\chi}\left(\|q^{n+1}\|^2 - \|q^n\|^2 - \|q^{n+1} - q^n\|^2\right)
\end{aligned}$$

$$q^{n+1}\|^2 - \|q^n\|^2) - \chi\Delta t\|\nabla\cdot\tilde{\mathbf{u}}^{n+1}\|^2. \tag{60}$$

Next we take the L^2 inner product between (55) and $2\mathbf{u}^{n+1}$ to obtain

$$\|\mathbf{u}^{n+1}\|^2 - \|\tilde{\mathbf{u}}^{n+1}\|^2 + \|\mathbf{u}^{n+1} - \tilde{\mathbf{u}}^{n+1}\|^2 = 0. \tag{61}$$

Combining the above four relations leads to

$$\|E^{n+1}\|^2 + \|\tilde{\mathbf{u}}^{n+1} - \mathbf{u}^n\|^2 + \Delta t\left(2\nu\|\nabla\tilde{\mathbf{u}}^{n+1}\|^2 - \chi\|\nabla\cdot\tilde{\mathbf{u}}^{n+1}\|^2\right) \leqslant \|E^n\|^2, \tag{62}$$

where

$$\|E^k\|^2 := \|\mathbf{u}^k\|^2 + \Delta t^2\|\nabla\psi^k\|^2 + \frac{\Delta t}{\chi}\|q^k\|^2.$$

We recall that

$$\|\nabla\cdot\mathbf{u}\|^2 \leqslant d\|\nabla\mathbf{u}\|^2, \quad \forall u \in H^1(\Omega)^d, \tag{63}$$

where d is the dimension of the domain. Hence, we can conclude from the above that

Theorem 1. *Let $0 < \chi \leqslant \frac{2\nu}{d}$. Then the scheme (50a)–(51d) is unconditionally stable, and we have*

$$\|\mathbf{u}^{n+1}\|^2 + \Delta t^2\|\nabla\psi^{n+1}\|^2 + \frac{\Delta t}{\chi}\|q^{n+1}\|^2 + \Delta t(2\nu - \chi d)\|\nabla\tilde{\mathbf{u}}^{n+1}\|^2 \leqslant \|\mathbf{u}^n\|^2 + \Delta t^2\|\nabla\psi^n\|^2 + \frac{\Delta t}{\chi}\|q^n\|^2.$$

5. Concluding remarks

We have presented a generalized form of open/outflow boundary conditions for incompressible flows and a pressure correction-based algorithm for numerically treating these open boundary conditions. The generalized form represents a family of open boundary conditions, with the characteristic that they all ensure the energy stability of the system. These open boundary conditions are effective even when strong backflows or vortices occur at the open/outflow boundaries. Our algorithm is based on a rotational pressure-correction strategy, and introduces an auxiliary variable and an associated discrete equation together with boundary conditions. The formulation allows for the direct computation of the pressure in the $H^1(\Omega)$ space. The algorithm imposes on the open boundary a pressure Dirichlet type condition in the pressure substep and a velocity Neumann type condition in the velocity substep. The current algorithm can work properly with equal orders of approximation for the pressure and the velocity.

In addition to the above algorithm, which is semi-implicit and conditionally stable in nature, for a sub-class of the generalized form of open boundary conditions we have also developed an unconditionally stable scheme and provided a proof for its unconditional stability.

Extensive numerical experiments have been presented for several problems involving outflow/open boundaries for a range of Reynolds numbers. We have compared the current simulation results with the experimental data from the literature, as well as with the existing numerical simulations by other researchers, to demonstrate the accuracy of the method developed in this work. We have also shown that our method produces long-time stable simulations at moderate and high Reynolds numbers when strong vortices and backflows occur at the open/outflow boundaries. By contrast, usual outflow boundary conditions such as the traction-free condition or the no-flux condition encounters numerical difficulties at these Reynolds numbers, and the computation blows up instantly when the vortices hit the open boundary.

Among the six open boundary conditions we have studied more closely, according to the energy balance equation, with OBC-A, OBC-E and OBC-F the power contributed by the fluid stress on the outflow boundary locally exactly balances the kinetic energy influx into the domain in the backflow regions. In contrast, with OBC-B, OBC-C and OBC-D the power contributed by the fluid stress in the backflow regions of the open boundary induces an extra dissipation to the total kinetic energy, while locally balancing the kinetic energy influx into the domain. In such a sense the boundary conditions OBC-B, OBC-C and OBC-D are more energy-dissipative. The numerical experiments indicate little quantitative difference in term of the numerical errors or the global physical quantities between these more dissipative boundary conditions and the other three less dissipative ones. On the other hand, in terms of the more qualitative aspects such as the velocity patterns and the discharge of vortices through the open boundary, our observation seems to suggest that the more dissipative open boundary conditions appear preferable. Among the three more dissipative ones, the open boundary condition OBC-C appears more favorable in terms of the distortion caused to the vortices while crossing the outflow boundary.

The numerical instability associated with strong vortices or backflows at the open/outflow boundaries are widely encountered in flow problems involving physically unbounded domains. The method developed in the current work provides an effective means for overcoming this instability. It provides the opportunity for using a substantially smaller computational domain in numerical simulations than otherwise for problems on physically unbounded domains. The domain size can be chosen solely based on the consideration of physical accuracy. The ability to use a substantially smaller computational domain will facilitate simulations at high Reynolds numbers, because of the increased grid resolution under identical will be instrumental in numerical simulations at Reynolds numbers significantly higher than

Acknowledgements

S.D. would like to acknowledge the support from NSF (DMS-1318820) and ONR (N000141110028). J.S. would like to acknowledge the support from NSF (DMS-1217066 and DMS-1419053).

References

[1] I. Babuska, The finite element method with Lagrangian multipliers, Numer. Math. 20 (1973) 179–192.
[2] Y. Bazilevs, J.R. Hohean, T.J.R. Hughes, R.D. Moser, Y. Zhang, Patient-specific isogeometric fluid–structure interaction analysis of thoracic aortic blood flow due to implantation of the Jarvik 2000 left ventricular assist device, Comput. Methods Appl. Mech. Eng. 198 (2009) 3534–3550.
[3] P. Beaudan, P. Moin, Numerical experiments on the flow past a circular cylinder at sub-critical Reynolds numbers, Report No. TF-62, Thermal Sciences Division, Department of Mechanical Engineering, Stanford University, 1994.
[4] M. Behr, J. Liou, R. Shih, T.E. Tezduyar, Vorticity-streamfunction formulation of unsteady incompressible flow past a cylinder: sensitivity of the computed flow field to the location of the outflow boundary, Int. J. Numer. Methods Fluids 12 (1991) 323–342.
[5] C. Bertoglio, A. Caiazzo, A tangential regularization method for backflow stabilization in hemodynamics, J. Comput. Phys. 261 (2014) 162–171.
[6] M. Braza, P. Chassaing, H. Ha Minh, Numerical study and physical analysis of the pressure and velocity fields in the near wake of a circular cylinder, J. Fluid Mech. 165 (1986) 79–130.
[7] F. Brezzi, On the existence, uniqueness and approximation of saddle-point problems arising from Lagrangian multipliers, ESAIM: Math. Model. Numer. Anal. 8 (1974) 129–151.
[8] C.-H. Bruneau, P. Fabrie, Effective downstream boundary conditions for incompressible Navier–Stokes equations, Int. J. Numer. Methods Fluids 19 (1994) 693–705.
[9] C.-H. Bruneau, P. Fabrie, New efficient boundary conditions for incompressible Navier–Stokes equations: a well-posedness result, Math. Model. Numer. Anal. 30 (1996) 815–840.
[10] J. Craske, M. van Reeuwijk, Robust and accurate open boundary conditions for incompressible turbulent jets and plumes, Comput. Fluids 86 (2013) 284–297.
[11] N.K. Delany, N.E. Sorenson, NACA Tech. Note 3038, 1953.
[12] S. Dong, An outflow boundary condition and algorithm for incompressible two-phase flows with phase field approach, J. Comput. Phys. 266 (2014) 47–73.
[13] S. Dong, G.E. Karniadakis, DNS of flow past stationary and oscillating cylinder at $Re = 10{,}000$, J. Fluids Struct. 20 (2005) 14–23.
[14] S. Dong, G.E. Karniadakis, C. Chryssostomidis, A robust and accurate outflow boundary condition for incompressible flow simulations on severely-truncated unbounded domains, J. Comput. Phys. 261 (2014) 83–105.
[15] S. Dong, G.E. Karniadakis, A. Ekmekci, D. Rockwell, A combined DNS–PIV study of the turbulent near wake, J. Fluid Mech. 569 (2006) 185–207.
[16] S. Dong, J. Shen, An unconditionally stable rotational velocity-correction scheme for incompressible flows, J. Comput. Phys. 229 (2010) 7013–7029.
[17] M.S. Engelman, M.-A. Jamnia, Transient flow past a circular cylinder: a benchmark solution, Int. J. Numer. Methods Fluids 11 (1990) 985–1000.
[18] E. Ferrer, D. Moxey, R.H.J. Willden, S.J. Sherwin, Stability of projection methods for incompressible flows using high order pressure–velocity pairs of same degree: continuous and discontinuous Galerkin formulations, Commun. Comput. Phys. 16 (2014) 817–840.
[19] R.K. Finn, Determination of the drag on a cylinder at low Reynolds numbers, J. Appl. Phys. 24 (1953) 771–773.
[20] M.Y. Forestier, R. Pasquetti, R. Peuret, C. Sabbah, Spatial development of wakes using a spectral multi-domain method, Appl. Numer. Math. 33 (2000) 207–216.
[21] L. Formaggia, J.-F. Gerbeau, F. Nobile, A. Quarteroni, Numerical treatment of defective boundary conditions for the Navier–Stokes equations, SIAM J. Numer. Anal. 40 (2002) 376–401.
[22] R. Franke, W. Rodi, B. Schonung, Numerical calculation of laminar vortex-shedding flow cylinders, J. Wind Eng. Ind. Aerodyn. 35 (1990) 237–257.
[23] D.K. Gartling, A test problem for outflow boundary conditions – flow over a backward-facing step, Int. J. Numer. Methods Fluids 11 (1990) 953–967.
[24] V. Gravemeier, A. Comerford, L. Yoshihara, M. Ismail, W.A. Wall, A novel formulation for Neumann inflow boundary conditions in biomechanics, Int. J. Numer. Methods Biomed. Eng. 28 (2012) 560–573.
[25] P.M. Gresho, Incompressible fluid dynamics: some fundamental formulation issues, Annu. Rev. Fluid Mech. 23 (1991) 413–453.
[26] D.F. Griffiths, The 'no boundary condition' outflow boundary condition, Int. J. Numer. Methods Fluids 24 (1997) 393–411.
[27] L. Grinberg, G.E. Karniadakis, Outflow boundary conditions for arterial networks with multiple outlets, Ann. Biomed. Eng. 36 (2008) 1496–1514.
[28] J.-L. Guermond, L. Quartapelle, On stability and convergence of projection methods based on pressure Poisson equation, Int. J. Numer. Methods Fluids 26 (1998) 1039–1053.
[29] J.L. Guermond, P. Minev, J. Shen, Error analysis of pressure-correction schemes for the time-dependent Stokes equations with open boundary conditions, SIAM J. Numer. Anal. 43 (2005) 239–258.
[30] J.L. Guermond, P. Minev, J. Shen, An overview of projection methods for incompressible flows, Comput. Methods Appl. Mech. Eng. 195 (2006) 6011–6045.
[31] J.L. Guermond, J. Shen, A new class of truly consistent splitting schemes for incompressible flows, J. Comput. Phys. 192 (2003) 262–276.
[32] J.L. Guermond, J. Shen, Velocity-correction projection methods for incompressible flows, SIAM J. Numer. Anal. 41 (2003) 112–134.
[33] J.L. Guermond, J. Shen, On the error estimates for the rotational pressure-correction projection methods, Math. Comput. 73 (2004) 1719–1737.
[34] N. Hasan, S.F. Anwer, S. Sanghi, On the outflow boundary condition for external incompressible flows: a new approach, J. Comput. Phys. 206 (2005) 661–683.
[35] J.G. Heywood, R. Rannacher, S. Turek, Artificial boundaries and flux and pressure: conditions for the incompressible Navier–Stokes equations, Int. J. Numer. Methods Fluids 22 (1996) 325–352.
[36] R.R. Hwang, S.H. Lin, On laminar wakes behind a circular cylinder in stratified fluids, ASME J. Fluids Eng. 114 (1992) 20–28.
[37] M. Ismail, V. Gravemeier, A. Comerford, W.A. Wall, A stable approach for coupling multidimensional cardiovascular and pulmonary networks based on a novel pressure-flow rate or pressure-only Neumann boundary condition formulation, Int. J. Numer. Methods Biomed. Eng. 30 (2014) 447–469.
[38] G. Jin, M. Braza, A nonreflecting outlet boundary condition for incompressible unsteady Navier–Stokes calculations, J. Comput. Phys. 107 (1993) 239–253.
[39] B.C.V. Johansson, Boundary conditions for open boundaries for the incompressible Navier–Stokes equation, J. Comput. Phys. 105 (1993) 233–251.
[40] G.E. Karniadakis, Numerical simulation of forced convection heat transfer from a cylinder in crossflow, Int. J. Heat Mass Transf. 31 (1988) 107–118.
[41] G.E. Karniadakis, M. Israeli, S.A. Orszag, High-order splitting methods for the incompressible Navier–Stokes equations, J. Comput. Phys. 97 (1991) 414–443.
[42] G.E. Karniadakis, S.J. Sherwin, Spectral/hp Element Methods for Computational Fluid Dynamics, 2nd edn., Oxford University Press, 2005.
f a laminar backward-facing step flow at $Re = 800$ with a spectral domain decomposition method, Int. J. Numer.

[44] H.J. Kim, C.A. Figueroa, T.J.R. Hughes, K.E. Jansen, C.A. Taylor, Augmented Langrangian method for constraining the shape of velocity profiles at outlet boundaries for three-dimensional finite element simulations of blood flow, Comput. Methods Appl. Mech. Eng. 198 (2009) 3551–3566.
[45] L.I.G. Kovasznay, Laminar flow behind a two-dimensional grid, Proc. Camb. Philol. Soc. 44 (1948) 58.
[46] A.G. Kravchenko, P. Moin, K. Shariff, B-spline method and zonal grids for simulations of complex turbulent flows, J. Comput. Phys. 151 (1999) 757–789.
[47] O.A. Ladyzhenskaya, The Mathematical Theory of Viscous Incompressible Flow, 2nd edition, Gordon and Breach, New York, 1969.
[48] M. Lanzendorfer, J. Stebel, On pressure boundary conditions for steady flows of incompressible fluids with pressure and shear rate dependent viscosities, Appl. Math. 56 (2011) 265–285.
[49] J.M. Leone, Open boundary condition symposium benchmark solution: stratified flow over a backward-facing step, Int. J. Numer. Methods Fluids 11 (1990) 969–984.
[50] J. Liu, Open and traction boundary conditions for the incompressible Navier–Stokes equations, J. Comput. Phys. 228 (2009) 7250–7267.
[51] J.-G. Liu, J. Liu, R.L. Pego, Stability and convergence of efficient Navier–Stokes solvers via a commutator estimate, Commun. Pure Appl. Math. LX (2007) 1443–1487.
[52] X. Ma, G.-S. Karamanos, G.E. Karniadakis, Dynamics and low-dimensionality of a turbulent near wake, J. Fluid Mech. 410 (2000) 29–65.
[53] J.R. Meneghini, P.W. Bearman, Numerical simulation of high amplitude oscillatory-flow about a circular cylinder using a discrete vortex method, in: AIAA Shear Flow Conference, Orlando, FL, 1993, pp. 1–11, AIAA Paper 93-3288.
[54] M.E. Moghadam, Y. Bazilevs, T.-Y. Hsia, I.E. Vignon-Clementel, A.L. Marsden, A comparison of outlet boundary treatments for prevention of backflow divergence with relevance to blood flow simulations, Comput. Mech. 48 (2011) 277–291.
[55] D.J. Newman, G.E. Karniadakis, Direct numerical simulations of flow over a flexible cable, in: Proceedings of 6th International Conference on Flow-Induced Vibrations, 1995, pp. 193–203.
[56] D.J. Newman, G.E. Karniadakis, Simulations of flow over a flexible cable: a comparison of forced and flow-induced vibration, J. Fluids Struct. 10 (1996) 439–454.
[57] C. Norberg, Fluctuating lift on a circular cylinder: review and new measurements, J. Fluids Struct. 17 (2003) 57–96.
[58] J. Nordstrom, K. Mattsson, C. Swanson, Boundary conditions for a divergence free velocity-free formulation of the Navier–Stokes equations, J. Comput. Phys. (2007) 874–890.
[59] J. Nordstrom, M. Svard, Well-posed boundary conditions for the Navier–Stokes equations, SIAM J. Numer. Anal. 43 (2005) 1231–1255.
[60] M.A. Olshanskii, V.M. Staroverov, On simulation of outflow boundary conditions in finite difference calculations for incompressible fluid, Int. J. Numer. Methods Fluids 33 (2000) 499–534.
[61] I. Orlanski, A simple boundary condition for unbounded hyperbolic flows, J. Comput. Phys. 21 (1976) 251–269.
[62] T.C. Papanastasiou, N. Malamataris, K. Ellwood, A new outflow boundary condition, Int. J. Numer. Methods Fluids 14 (1992) 587–608.
[63] H. Persillon, M. Braza, Physical analysis of the transition to turbulence in the wake of a circular cylinder by three-dimensional Navier–Stokes simulation, J. Fluid Mech. 365 (1998) 23–88.
[64] A. Poux, S. Glockner, E. Ahusborde, M. Azaiez, Open boundary conditions for the velocity-correction scheme of the Navier–Stokes equations, Comput. Fluids 70 (2012) 29–43.
[65] A. Poux, S. Glockner, M. Azaiez, Improvements on open and traction boundary conditions for Navier–Stokes time-splitting methods, J. Comput. Phys. 230 (2011) 4011–4027.
[66] M. Renardy, Imposing 'no' boundary condition at outflow: why does it work?, Int. J. Numer. Methods Fluids 24 (1997) 413–417.
[67] A. Roshko, Experiments on the flow past a circular cylinder at very high Reynolds numbers, J. Fluid Mech. 10 (1961) 345–356.
[68] M.R. Ruith, P. Chen, E. Meiburg, Development of boundary conditions for direct numerical simulations of three-dimensional vortex breakdown phenomena in semi-infinite domains, Comput. Fluids 33 (2004) 1225–1250.
[69] R.L. Sani, P.M. Gresho, Resume and remarks on the open boundary condition minisymposium, Int. J. Numer. Methods Fluids 18 (1994) 983–1008.
[70] S.J. Sherwin, G.E. Karniadakis, A triangular spectral element method: applications to the incompressible Navier–Stokes equations, Comput. Methods Appl. Mech. Eng. 123 (1995) 189–229.
[71] S. Tang, N. Audry, On the symmetry breaking instability leading to vortex shedding, Phys. Fluids 9 (1997) 2550–2561.
[72] S. Taylor, J. Rance, J.O. Medwell, A note on the imposition of traction boundary conditions when using the FEM for solving incompressible flow problems, Commun. Appl. Numer. Methods 1 (1985) 113–121.
[73] L.J.P. Timmermans, P.D. Minev, F.N. van de Vosse, An approximate projection scheme for incompressible flow using spectral elements, Int. J. Numer. Methods Fluids 22 (1996) 673–688.
[74] D.J. Tritton, Experiments on the flow past a circular cylinder at low Reynolds numbers, J. Fluid Mech. 6 (1959) 547.
[75] S.V. Tsynkov, Numerical solution of problems on unbounded domains: a review, Appl. Numer. Math. 27 (1998) 465–532.
[76] C. Wieselsberger, Recent statements on the laws of liquid and air resistancy, Phys. Z. 22 (1921) 321–328.
[77] C.H.K. Williamson, Vortex dynamics in a cylinder wake, Annu. Rev. Fluid Mech. 28 (1996) 477–539.
[78] H.Q. Zhang, U. Fey, B.R. Noack, M. Konig, H. Engelmann, On the transition of the cylinder wake, Phys. Fluids 7 (1995) 779–793.
[79] J. Zhang, C. Dalton, A three-dimensional simulation of a steady approach flow past a circular cylinder at low Reynolds number, Int. J. Numer. Methods Fluids 26 (1998) 1003–1022.
[80] X. Zheng, S. Dong, An eigen-based high-order expansion basis for structured spectral elements, J. Comput. Phys. 230 (2011) 8573–8602.